RSC Advances

PAPER

View Article Online
View Journal | View Issue

Cite this: *RSC Adv.*, 2026, **16**, 25944

Targeted delivery of gemcitabine to lung cancer cells *via* a hyaluronic acid-based nanoplatform

Fengbo Yu,[ab] Jingdan Cao,[b] Xingjun Fan,[d] Junxia Gao,[c] Guifang Liu,[b] Chonghuan Lin,[b] Ying Zhu[b] and Qiang Wang *[c]

To mitigate the dose-limiting toxicity of gemcitabine (GEM) in lung cancer therapy, we developed a targeted hyaluronic acid (HA)-based nanoplatform with sustained drug-release capabilities—GEM@HA-(HAP/PSI). The system consisted of a hydroxyapatite/polysuccinimide (HAP/PSI) composite core for efficient drug loading, with surface-conjugated HA serving as a CD44-targeting ligand. Following systematic optimization using response surface methodology, the resulting spherical nanoparticles (~100–200 nm) exhibited pH-responsive drug release, good biocompatibility, and negligible hemolytic activity. *In vitro* studies using CD44-high A549 and CD44-low H358 cells confirmed that CD44-mediated active endocytosis was the predominant uptake pathway for the nanoplatform. Treatment with the optimized formulation (GEM@HA-(HAP/PSI)$_{10}$) led to significantly greater cytotoxicity, inhibition of cell migration and colony formation, and apoptosis induction than treatment with a non-targeted control formulation. Importantly, in A549 xenograft mouse models, GEM@HA-(HAP/PSI)$_{10}$ achieved superior tumor growth suppression relative to free GEM while also maintaining a favorable safety profile. Collectively, these findings indicate that the HA-targeted nanoplatform developed in this study enhances the precision and therapeutic efficacy of GEM delivery and holds promise for reducing its systemic toxicity.

Received 11th March 2026
Accepted 1st May 2026

DOI: 10.1039/d6ra02076c

rsc.li/rsc-advances

1. Introduction

Lung cancer remains a critical global public health challenge. According to the 2022 Global Cancer Statistics (GLOBOCAN) released by the International Agency for Research on Cancer (IARC), cancer was responsible for an estimated 9.67 million deaths worldwide, accounting for approximately 250 million disability-adjusted life years.[1] Notably, China bears the highest burden of this disease globally, with lung cancer exhibiting the highest incidence (1.06 million new cases) and mortality (733 300 deaths) among all cancer types.[2] Current clinical management strategies for lung cancer include surgical resection, targeted therapy, immunotherapy, chemotherapy, and radiotherapy. Surgery can provide a 5-year survival rate of 40–80% in patients with early-stage disease. However, owing to the insidious onset of lung cancer, approximately 70% of patients are diagnosed at locally advanced or metastatic stages, at which point curative surgery is often no longer feasible.[3] In cases of advanced disease, systemic pharmacotherapy remains the primary treatment strategy. Although targeted agents are initially effective in genetically eligible patients, therapeutic resistance almost inevitably emerges. Consequently, chemotherapy continues to serve as a cornerstone of treatment for most patients with advanced lung cancer in order to control tumor progression and prolong survival.[4] One major limitation of conventional chemotherapy is the lack of selectivity, which often leads to severe damage in healthy tissues, dose-limiting toxicities, the development of drug resistance, and frequent treatment discontinuation.[5] Therefore, there is an urgent need to develop efficient, target-specific, safe, and clinically translatable drug delivery systems. Such platforms could enable the precise intracellular delivery of chemotherapeutic agents, thereby minimizing off-target effects, lowering required dosages, enhancing therapeutic efficacy, and potentially accelerating anticancer drug development.

Nanotechnology presents a promising solution for addressing these challenges. Nanocarrier-based drug delivery systems (NDDSs) have attracted considerable attention in biomedicine due to their ability to facilitate targeted delivery and controlled drug release.[6] The high surface-to-volume ratio of nanomaterials enables functionalization with targeting ligands, thereby improving tumor selectivity.[7] Through encapsulation, adsorption, and the conjugation of therapeutic agents, NDDSs can enhance the bioavailability of poorly soluble drugs and promote their preferential accumulation in tumor tissues *via*

[a]*Collaborative Innovation Center for Development and Application of Northern Medicine Resources, Mudanjiang Medical University, Mudanjiang, Heilongjiang Province, People's Republic of China*
[b]*School of Pharmacy, Mudanjiang Medical University, Mudanjiang, Heilongjiang Province, People's Republic of China*
[c]*Hongqi Hospital, Mudanjiang Medical University, Mudanjiang, Heilongjiang Province, People's Republic of China*
[d]*School of Public Health, Mudanjiang Medical University, Mudanjiang, Heilongjiang Province, People's Republic of China. E-mail: drwang1982@126.com*

the enhanced permeability and retention (EPR) effect, ultimately improving therapeutic outcomes while reducing systemic toxicity. Furthermore, NDDSs can help overcome multidrug resistance (MDR)—a major contributor to chemotherapy failure—by bypassing efflux pumps, targeting cancer stem cells (CSCs), and modulating the tumor microenvironment.[8] Owing to these advancements, NDDSs are emerging as transformative tools in clinical oncology, driving progress in targeted therapy, combination treatment strategies, and early cancer diagnostics.[9]

Targeting strategies for NDDSs can broadly be classified as passive, active, or stimulus-responsive. Passive targeting exploits the EPR effect, whereby nanocarriers preferentially extravasate through the leaky vasculature of tumor tissues and are retained due to deficient lymphatic drainage.[10] However, the EPR effect exhibits substantial inter- and intratumoral heterogeneity, and high interstitial fluid pressure within tumors can impede deep nanocarrier penetration. To overcome these limitations, active targeting strategies have been developed. These strategies involve the functionalization of nanocarriers with targeting ligands (*e.g.*, antibodies, peptides, or polysaccharides) that selectively bind to receptors overexpressed on cancer cells.[11] Subsequently, ligand–receptor interactions facilitate receptor-mediated endocytosis and intracellular drug release, thereby enhancing tumor specificity and intracellular accumulation while minimizing uptake by healthy tissues. Among potential targets, the CD44 receptor, a transmembrane glycoprotein, has emerged as a promising target for active delivery. CD44 is overexpressed in a wide range of cancers, including most lung cancers, and plays a key role in tumor initiation, progression, metastasis, and therapeutic resistance.[12] In contrast, in normal tissues, CD44 is expressed at low levels or is functionally inactive. Hyaluronic acid (HA), a major component of the extracellular matrix, is a natural ligand for CD44, and the CD44–HA interaction is crucially involved in tumor progression and metastasis. Accordingly, HA-modified nanocarriers can selectively bind to CD44-overexpressing cancer cells, promoting tumor-specific drug delivery, enhancing intracellular uptake, and reducing off-target toxicity.[13] In addition, HA is biocompatible, biodegradable, and non-immunogenic, and has been widely employed in both clinical and experimental applications, including drug delivery and biomedical imaging.[14] Targeting CD44 *via* HA therefore holds considerable promise not only for drug delivery but also for tumor imaging and theranostic applications.

In this study, we developed an HA-based targeted NDDS using hydroxyapatite (HAP) and polysuccinimide (PSI) as core materials. HAP, the primary inorganic constituent of bone, exhibits excellent biocompatibility, bioactivity, and high drug-loading capacity.[15,16] Meanwhile, PSI is an amorphous, biodegradable, and nontoxic polymer synthesized *via* solvent-free polycondensation of aspartic acid, aligning with green chemistry principles.[17] Importantly, PSI can be readily functionalized through amine-induced ring-opening reactions, enabling the introduction of targeting moieties while maintaining biodegradability.[18,19] In contrast to conventional nanocarriers (*e.g.*, liposomes or polymeric micelles), which typically exhibit low drug-loading capacity, complex synthesis,[20] poor colloidal stability, and scale-up bottlenecks,[21] the HAP/PSI hybrid system uniquely combines high drug-loading capacity, good biocompatibility, and facile surface functionalization. However, existing HAP/PSI-based systems lack active tumor targeting, and no study has yet exploited CD44-mediated delivery using hyaluronic acid (HA) functionalization on such hybrid nanoparticles for lung cancer therapy. To address this gap, our group has previously demonstrated that PSI and its derivatives (X-PSI) can co-assemble with HAP to form uniform nanoparticles (HAP/PSI or X-(HAP/PSI)) with efficient drug-loading capabilities.[22] Building on this foundation, the core research idea of the present work is to conjugate HA—a natural ligand for CD44 overexpressed on lung cancer cells—to PSI, generating a targeting polymer (HA–PSI), which is then co-assembled with HAP to produce core–shell nanoparticles designated as HA-(HAP/PSI). This nanoplatform was loaded with gemcitabine (GEM), a first-line chemotherapeutic agent for lung cancer. GEM is a nucleoside analog that, following intracellular activation, inhibits DNA synthesis and induces apoptosis.[23] However, its clinical application is limited by dose-limiting adverse effects, including myelosuppression and gastrointestinal toxicity. We hypothesized that the GEM@HA-(HAP/PSI) system would enhance the tumor-specific delivery of GEM *via* CD44-mediated endocytosis, enable controlled intracellular drug release, reduce nonspecific distribution in healthy tissues, and ultimately improve the therapeutic index of GEM in lung cancer therapy.

2. Materials and methods

2.1. Materials

All chemicals and reagents were of analytical grade or higher and were used as received. Tween-80 was purchased from BioFroxx Co., Ltd. Butyl acetate, calcium chloride, phosphoric acid, sodium carbonate, disodium hydrogen phosphate, *N*,*N*-dimethylformamide, *N*,*N*-dimethylacetamide, dichloromethane, and acetonitrile were obtained from Tianjin Hengxing Chemical Reagent Manufacturing Co., Ltd, Harbin Reagent Chemical Plant, Tianjin Tianli Chemical Reagent Co., Ltd, Tianjin Bodi Chemical Co., Ltd, Tianjin Fuyu Fine Chemical Co., Ltd, and Tianjin Yongda Chemical Reagent Co., Ltd, respectively. L-Aspartic acid was supplied by Aladdin Co., Ltd. Gemcitabine hydrochloride, potassium bromide, 1,6-hexanediamine, and coumarin 6 were acquired from Shanghai Macklin Biochemical Technology Co., Ltd. Hyaluronic acid (HA, $M_w \approx 3000$ Da) was purchased from Shanghai Eon Chemical Technology Co., Ltd. MES buffer, EDCI, and NHS were sourced from Shanghai Yuanye Bio-Technology Co., Ltd.

For cell culture and *in vitro* studies, fetal bovine serum (FBS) was procured from Sino Biological Inc.; trypsin, phosphate-buffered saline (PBS), penicillin–streptomycin (100×), Cell Counting Kit-8 (CCK-8), DAPI staining solution, 4% paraformaldehyde fixative, and anti-fade mounting medium were obtained from Seven Innovation (Beijing) Biotech Co., Ltd; RPMI 1640 medium was from Thermo Fisher Scientific Inc.; crystal violet stain, Hoechst 33 342, and DAPI were from Beyotime Biotechnology Co., Ltd; and Calcein-AM/PI double stain kit

was from Solarbio Science & Technology Co., Ltd. The endocytosis inhibitors chlorpromazine, indomethacin, and colchicine were purchased from MedChemExpress.

For *in vivo* and histology studies, a 2% red blood cell suspension was provided by Guangzhou Hongquan Biotechnology Co., Ltd; clinical-grade gemcitabine hydrochloride for injection (Lot: 246962DP) was from Eli Lilly and Company; hematoxylin and eosin (H&E) staining reagents were from Shanghai Titan Technology Co., Ltd; absolute ethanol, xylene, potassium dihydrogen phosphate, disodium hydrogen phosphate, sodium chloride, and potassium chloride were supplied by Sinopharm Chemical Reagent Co., Ltd; and the TUNEL apoptosis assay kit was purchased from Vazyme Biotech Co., Ltd.

2.2. Animals and ethics statement

Male BALB/c nude mice (8 weeks old, 20–25 g) were supplied by Sibeifu (Beijing) Biotechnology Co., Ltd and housed under specific pathogen-free (SPF) conditions. The animal room was maintained at 23 ± 3 °C with 30–70% relative humidity under a 12 h light/dark cycle, with free access to standard rodent diet and water. All animal procedures were performed in accordance with the Guidelines for Care and Use of Laboratory Animals of Mudanjiang Medical University and approved by the Animal Ethics Committee of Mudanjiang Medical University (approval no. IACUC-20251015-303).

2.3. Methods

2.3.1. Synthesis of excipients

2.3.1.1. Preparation of HAP and PSI. HAP and PSI were synthesized according to the methods reported in our previous study.[22]

2.3.1.2. Preparation of HA–PSI conjugates

2.3.1.2.1 Synthesis of HA–NH_2. HA powder (0.5 g, ~0.17 mmol, $M_w \approx 3000$ Da) was dissolved in 20 mL of MES buffer, with stirring, at room temperature (about 25 °C). Then, EDCI (0.095 g, 0.495 mmol) and NHS (0.057 g, 0.495 mmol) were added sequentially to this solution. After activation for 2 h, 1,6-hexanediamine (0.038 g, 0.33 mmol) was added. The reaction mixture was stirred continuously for 24 h at room temperature.[24] The product was then transferred to a dialysis bag (M_w: 1000 Da) and dialyzed against deionized water for 24 h to remove excess reagents and buffer salts. The purified solution was lyophilized (FDS-1000, Tokyo Rikakikai Co., Ltd) to obtain the amine-functionalized HA (HA–NH_2).

2.3.1.2.2 Conjugation of HA–NH_2 to PSI. PSI (M_w calculated based on the repeating unit $-C_4H_3NO_2^- = 97.07$) was dissolved in anhydrous *N*,*N*-dimethylformamide (DMF) at a concentration of 6 mg mL^{-1}. To achieve different molar feed ratios of HA to PSI, varying amounts of PSI were used: 0.03 g (0.31 mmol) for a 1 : 10 ratio (denoted as HA–PSI_{10}), 0.06 g (0.62 mmol) for a 1 : 20 ratio (HA–PSI_{20}), and 0.12 g (1.24 mmol) for a 1 : 40 ratio (HA–PSI_{40}). HA–NH_2 (0.10 g, ~0.03 mmol) was dissolved separately in each corresponding PSI/DMF solution. The mixtures were stirred at 65 °C for 18 h. Subsequently, each reaction mixture was dialyzed (M_w: 1000 Da) against deionized water for 48 h to remove DMF. The final aqueous solutions were lyophilized to obtain HA–PSI conjugates in the form of solid products. Among these, HA–PSI_{10} showed the highest HA incorporation per PSI chain, while HA–PSI_{40} exhibited the lowest.

2.3.1.3. Characterization. The chemical structures of the synthesized materials were characterized *via* Fourier-transform infrared (FTIR) spectroscopy using a Nicolet iS5 spectrometer (Thermo Fisher, USA). Spectra were recorded in the range of 400–4000 cm^{-1} at a resolution of 1 cm^{-1}. Proton nuclear magnetic resonance (^{1}H NMR) spectroscopy was performed on an Avance NEO 400 MHz spectrometer (Bruker) using dimethyl sulfoxide-d_6 (DMSO-d_6) as the solvent. Morphological examinations were conducted using scanning electron microscopy (SEM, S-4800, Hitachi High-Technologies Corporation). Meanwhile, thermal stability was analyzed *via* thermogravimetric analysis (TGA) and derivative thermogravimetry (DTG) on a STA 449 F5 Jupiter instrument (NETZSCH) under a nitrogen atmosphere (flow rate of 10 mL min^{-1}), with the temperature ramped from 30 to 800 °C at a rate of 10 °C min^{-1}. Crystallographic structures were assessed *via* X-ray diffraction (XRD) analysis on an XRD-7000 diffractometer (Shimadzu, Japan) using Cu Kα radiation ($\lambda = 1.5418$ Å) and scanning the 2θ range from 10° to 70° at a rate of $5^\circ \cdot min^{-1}$.

2.3.2. Formulation and optimization of the GEM-loaded nano drug delivery system

2.3.2.1. Determination of the optimal ratio for HA-(HAP/PSI) nanosphere self-assembly. Based on preliminary data, HA-(HAP/PSI) nano-formulations were prepared using different mass ratios of the coating material (HA–PSI_{40}, HA–PSI_{20}, or HA–PSI_{10}) to the core material (HAP) (6 : 1, 8 : 1, and 10 : 1) in order to identify the optimal proportion for nanosphere fabrication. The shell-forming material (HA–PSI) was first dissolved in DMF at a concentration of 25 mg mL^{-1} under ultrasonication (40 kHz) to obtain a clear solution. Separately, a HAP suspension was prepared in distilled water. The HA–PSI/DMF solution was added dropwise to the HAP suspension at room temperature under continuous magnetic stirring at 1000 rpm. After addition was completed, the mixture was centrifuged at 12 000 rpm. The collected particles were washed repeatedly with distilled water and subsequently lyophilized for 8 h. The morphology of the resulting nanoparticles was characterized *via* SEM to determine the appropriate mass ratio for each HA–PSI type.

2.3.2.2. Single-factor experiments

2.3.2.2.1 Effect of drug concentration on encapsulation efficiency (EE) and drug loading capacity (DLC). The concentration of HAP was fixed at 5 mg mL^{-1}. Meanwhile, GEM was dissolved in distilled water to prepare solutions with concentrations of 5, 10, 20, 30, 40, and 50 mg mL^{-1}. Then, 25 mg of HAP was added to 5 mL of each drug solution. The mixtures were homogenized *via* ultrasonication (40 kHz, 2 min) and then allowed to stand for 10 min. The dispersions were subjected to high-speed centrifugation (12 000 rpm). The supernatant was collected, and the pellet was washed multiple times with small volumes of distilled water. The washings were combined with the supernatant and diluted to a fixed volume. The concentration of free, unencapsulated GEM in this solution was determined by

measuring the absorbance at 350 nm using a UV-2700i spectrophotometer (Shimadzu) against a standard calibration curve (Fig. S1). Each condition was tested in triplicate. The EE and DLC were calculated using the following formulas:

$$\text{EE}\ (\%) = (M_1/M_0) \times 100$$

$$\text{DLC}\ (\%) = M_1/(M_1 + M_2) \times 100$$

Here, M_1 is the mass of GEM loaded in the carrier, M_0 is the total mass of added GEM, and M_2 is the mass of the blank carrier.

2.3.2.2.2 Effect of HAP concentration on EE and DLC. The concentration of GEM was fixed at 40 mg mL^{-1}. Then, HAP concentrations were varied at 1, 2, 3, 5, 8, 10, and 15 mg mL^{-1}. The mixtures were processed as described above, and the EE and DLC were determined to optimize the HAP concentration range.

2.3.2.2.3 Effect of adsorption time on EE and DLC. A GEM solution (40 mg mL^{-1}) was prepared in a volumetric flask. Then, HAP was added to this solution to achieve a concentration of 5 mg mL^{-1}, followed by homogenization *via* ultrasonication (40 kHz, 2 min). Adsorption was allowed to proceed for 10, 20, 40, and 60 min. At each time point, the mixture was centrifuged, and the supernatant was processed for GEM quantification as described above. The EE and DLC were calculated, and samples from each time point were tested in triplicate.

2.3.2.3. Formulation and process optimization for GEM@(HAP/PSI) and GEM@HA-(HAP/PSI). Based on the results of single-factor experiments, a Box–Behnken Design (BBD) response surface methodology was employed to optimize the GEM@(HAP/PSI) formulation. The key factors were as follows: drug concentration (30–50 mg mL^{-1}), HAP concentration (3–8 mg mL^{-1}), and the mass ratio of PSI to HAP (3 : 1 to 8 : 1). Response surface plots were generated based on the experimental data to guide the selection of the final formulation.

For the targeted formulations GEM@HA-$(HAP/PSI)_{10}$, GEM@HA-$(HAP/PSI)_{20}$, and GEM@HA-$(HAP/PSI)_{40}$, a Central Composite Design (CCD) was implemented using Design Expert software (version 10.0.1). The influencing factors were GEM concentration (30–50 mg mL^{-1}) and HAP concentration (3–8 mg mL^{-1}), while the amount of the solid coating material HA–PSI (as determined in Section 2.2.2.1) was kept constant. The final optimized formulations were characterized through SEM, particle size distribution analysis, and zeta potential measurement using a Malvern Nano ZS instrument (Spectris China Ltd, Shanghai).

2.3.3. Evaluation of nanoparticle properties

2.3.3.1. In vitro drug release study. The *in vitro* drug release profile of the formulations was investigated under simulated physiological conditions. Briefly, 10 mg of the GEM-loaded nano-formulation was placed in a centrifuge tube containing buffer solutions of different pH values (5.0, 6.8, and 7.4; 10 mL). The tubes were incubated in a constant-temperature shaker at 37 ± 0.5 °C at an agitation speed of 100 rpm. At predetermined time intervals (1, 2, 4, 6, 12, 24, 48, and 72 h), samples were withdrawn in triplicate and centrifuged. The supernatant was collected, and the pellet was washed. The washings were combined with the supernatant, and the absorbance of the resultant solution was measured at 350 nm. The concentration of the released GEM was determined based on a standard calibration curve, and the drug release profile was determined.

2.3.3.2. Hemolysis assay. A 2% erythrocyte suspension was prepared. Subsequently, 22 centrifuge tubes (5 mL) were set up, with 2 mL of the erythrocyte suspension added to each tube. The positive control tube contained 2 mL of distilled water, and the negative control tube contained 2 mL of physiological saline (0.9% NaCl). The remaining tubes were divided into four experimental groups (five tubes per group, corresponding to different nano-formulations). Then, 0.1, 0.2, 0.3, 0.4, or 0.5 mL of a 5% suspension of the GEM nano-preparation was added to each experimental tube. The mixtures were gently homogenized and incubated in a constant-temperature water bath at 37 °C for 3 h. Following incubation, the tubes were centrifuged. The absorbance of the resulting supernatant was measured at 545 nm using a SpectraMax M3 microplate reader. The hemolysis rate was calculated as follows:

$$\text{Hemolysis rate}\ (\%) = (A - A_0)/(A_1 - A_0) \times 100\%,$$

where A, A_0, and A_1 represent the absorbance levels of the test, negative control, and positive control samples, respectively.

2.3.3.3. In vitro cytocompatibility and targeting

2.3.3.3.1 Cell culture. A549 cells (high CD44 expression) and NCI-H358 cells (low CD44 expression) were selected for the experiments. Complete growth medium for both cell lines was prepared by mixing RPMI-1640 medium, heat-inactivated fetal bovine serum (FBS), and a penicillin–streptomycin solution at a 100 : 10 : 1 ratio. Cells were cultured at 37 °C in a humidified incubator under 5% CO_2.

2.3.3.3.2 Blank carrier cytotoxicity assay. Cells in the logarithmic growth phase were seeded into 96-well plates at a density of 1×10^4 cells per well. After 24 h of incubation, the medium was replaced with 100 μL of fresh medium containing blank carriers ((HAP/PSI), HA-$(HAP/PSI)_{40}$, HA-$(HAP/PSI)_{20}$, or HA-$(HAP/PSI)_{10}$) at concentrations ranging from 2.5 to 25 μg mL^{-1}. After 24 h of incubation, cell viability was assessed using the CCK-8 assay according to the manufacturer's instructions. Absorbance was measured at 450 nm (OD_{450}).

2.3.3.3.3 Assessment of cell proliferation with the CCK-8 assay. Cells were treated with free GEM or GEM-loaded formulations (GEM@(HAP/PSI), GEM@HA-$(HAP/PSI)_{40/20/10}$) at equivalent drug concentrations (2.5–25 μg mL^{-1}) for 24 h. Subsequently, cell viability was determined using the CCK-8 assay as described above.

2.3.3.3.4 Cellular uptake study. Coumarin 6 (C6) was used as a fluorescent probe. C6-labeled nanoparticles were prepared by incorporating C6 into the PSI or HA–PSI solution prior to the assembly process. Meanwhile, A549 and H358 cells were seeded onto glass coverslips in 24-well plates. After attachment, the cells were treated with the fluorescently tagged formulations for 0.5, 2, 4, and 6 h. The cells were then fixed with 4%

paraformaldehyde, stained with DAPI, and imaged using fluorescence microscopy.

2.3.3.3.5 Study of cellular uptake mechanisms. A549 cells were seeded onto coverslips in 24-well plates (1×10^5 cells per well) and cultured for 24 h. After cell adhesion, the original medium was replaced with medium containing different endocytosis inhibitors: chlorpromazine (CPZ, 10 μg mL^{-1}), colchicine (8 μg mL^{-1}), or indomethacin (100 μM). Cells were pre-incubated with these inhibitors for 1 h. The inhibitor-containing medium was then discarded, and C6-labeled nanoparticles were added to the plates. After incubation, the drug-containing medium was removed, and cells were washed three times with phosphate-buffered saline (PBS). The cells were fixed with 4% paraformaldehyde for 15 min and washed with PBS, and their nuclei were stained with DAPI for 5 min. The intracellular fluorescence distribution was observed and imaged using fluorescence microscopy. Fluorescence intensity was analyzed using ImageJ software. Finally, the endocytosis efficiency was compared across different inhibitor-treated groups to determine the primary mechanism of cellular uptake.

2.3.4. *In vitro* pharmacodynamics study

2.3.4.1. Cell morphology analysis. Cells in the logarithmic growth phase were inoculated into 6-well plates and cultivated until an appropriate cell density was achieved. Medium containing equivalent drug concentrations of GEM, GEM@(HAP/PSI), GEM@HA-$(HAP/PSI)_{40}$, GEM@HA-$(HAP/PSI)_{20}$, or GEM@HA-$(HAP/PSI)_{10}$ was added to the plates, along with a blank control (medium only). Following 24 h of incubation at 37 °C under 5% CO_2, the medium was removed, the cells were carefully rinsed with PBS, and morphological alterations were examined using an inverted microscope.

2.3.4.2. Colony formation assay. Cells were seeded at a low density (1000 cells per well) in 6-well plates. After overnight culture, the cells were treated with serum-free medium containing different test formulations (GEM, GEM@(HAP/PSI), GEM@HA-$(HAP/PSI)_{40}$, GEM@HA-$(HAP/PSI)_{20}$, GEM@HA-$(HAP/PSI)_{10}$). A control group was treated with drug-free, serum-free medium. Cell status was monitored daily. After 15 days of continuous incubation, when visible colonies (containing ≥50 cells) had formed, the experiment was terminated. The medium was removed, and cells were fixed with 4% paraformaldehyde for 20 min before two washes with PBS. The cells were then stained with 0.1% crystal violet solution for 10 min in the dark at room temperature, washed again with PBS, and air-dried. Colony formation was then assessed.

2.3.4.3. Wound healing assay. Cells in the logarithmic phase were seeded into 6-well plates (6×10^5 cells per well). Upon reaching ~80% confluence, a uniform scratch was created across the cell monolayer in each well using a sterile 10 μL pipette tip. The initial scratch width (0 h) was recorded. The experimental groups were treated with serum-free medium containing the different drug formulations at equivalent concentrations, while the control group was treated with serum-free medium only. The cells were further incubated for 12 h and 24 h. Images of the scratch area were captured at 0, 12, and 24 h using an inverted microscope. The scratch area was measured using ImageJ, and the cell migration rate was calculated as follows:

$$\text{Migration rate} = [(A_0 - A_t)/A_0] \times 100\%,$$

where A_0 represents the scratch area at 0 hours (immediately after scratching), and A_t represents the scratch area at a specific time point (*e.g.*, 12 h or 24 h after scratching).

2.3.4.4. Hoechst staining assay. A549 cells in the logarithmic phase were seeded onto coverslips in 24-well plates (5×10^4 cells per well). After adhesion, the cells were treated with serum-free medium containing equivalent drug concentrations of the various formulations for 4 h. A control group of cells was treated with drug-free, serum-free medium. Subsequently, the medium was removed, the cells were washed twice with PBS, and fixed with 4% paraformaldehyde for 20 min at room temperature. The cells were then washed again and stained with Hoechst 33 342 fluorescent dye for 20 min in the dark. Nuclear morphological features indicative of apoptosis were finally observed under a fluorescence microscope.

2.3.4.5. Live/dead cell staining assay. Cells were seeded onto coverslips in 24-well plates (8×10^4 cells per well) and cultured for 24 h. The medium was then replaced with drug-free, serum-free medium (control) or serum-free medium containing equivalent drug concentrations of the various formulations. After incubation, the solutions were removed, and cells were stained using a mixture of Calcein-AM and Propidium Iodide (PI) for 20 min. Live (green, Calcein-AM-positive) and dead (red, PI-positive) cells were visualized and imaged using fluorescence microscopy.

2.3.5. *In vivo* pharmacodynamics study

2.3.5.1. Animal model establishment. A549 cells were cultured in RPMI-1640 medium supplemented with 10% FBS and 1% penicillin–streptomycin. Cells in the logarithmic growth phase were harvested and subcutaneously injected into the right axilla of Balb/c-NU nude mice to establish an ectopic xenograft tumor model.

2.3.5.2. Tumor inhibition experiment. When tumor volumes reached approximately 100 mm^3, tumor-bearing mice were randomly divided into three groups ($n = 6$ per group): a saline control group, a free GEM group, and a GEM@HA-$(HAP/PSI)_{10}$ group. Treatments were administered *via* tail vein injection every 2 days for a total of 14 days. Tumor sizes and body weights were measured regularly. After the final injection, all mice were euthanized. Their tumors and major organs were excised, weighed, and photographed for the analysis of tumor weight. Meanwhile, tissues were fixed in 4% paraformaldehyde for subsequent experiments.

2.3.5.3. Hematoxylin and eosin (H&E) staining. Fixed tumor and organ tissues were processed *via* dehydration, paraffin embedding, and sectioning. Tissue sections were sequentially deparaffinized in xylene (I, II, 20 min each), rehydrated through a graded ethanol series (100% I & II, 10 min; 90%, 5 min; 80%, 5 min; 70%, 5 min), and rinsed with distilled water. The sections were stained with hematoxylin for 5 min, rinsed with water, counterstained with eosin for 1–2 min, and rinsed again. Finally, the sections were dehydrated using an ascending

ethanol series, cleared with xylene, and mounted in neutral resin. The stained sections were examined under a light microscope.

2.3.5.4. TUNEL staining. Prepared tissue sections were deparaffinized and rehydrated as described above. Then, antigen retrieval was performed using proteinase K treatment, followed by washing with PBS (2–3 times). A TUNEL reaction mixture was applied to the sections, which were then incubated at 37 °C in the dark for 60 min. After washing with PBS (three times, 5 min each), the sections were mounted in anti-fade mounting medium containing DAPI. Apoptotic cells were detected and imaged using fluorescence microscopy.

3. Results and discussion

3.1. Structure of HA–PSI

Fig. 1A–E present the ^{1}H NMR spectra of different formulations, whose characteristic proton signals were unambiguously annotated. Peak a ($\delta = 1.48$ ppm, Fig. 1C–E) was ascribed to the methylene protons (–CH_2–) of the hexamethylenediamine spacer in the HA–PSI conjugate. Meanwhile, peak b ($\delta = 1.7$ ppm, Fig. 1A, C–E) arose from the methyl protons (–$NHCOCH_3$) of the *N*-acetyl group in the HA backbone.[25] The split signals denoted as peak c ($\delta = 2.69$ ppm and 2.85 ppm, Fig. 1B–E) were assigned to the methylene protons (–CH_2–) of the PSI repeating unit, with the splitting pattern resulting from the adjacent chiral center.[26] Additionally, peak d ($\delta = 3.3$ ppm, Fig. 1A, C–E) corresponded to the protons on the glucuronic acid residue of HA. Meanwhile, peak f ($\delta = 5.25$ ppm, Fig. 1B–E) was attributed to the methine proton (–CH–) within the succinimide ring of PSI.[26] Notably, the appearance of a new peak e at $\delta = 4.5$ ppm (Fig. 1C–E) was observed, and its chemical shift was consistent with the methine proton adjacent to the newly formed amide linkage (–N–CH–C=O) in the HA–PSI conjugate.[27] These findings provided direct evidence for the successful conjugation of HA and PSI.

The FT-IR spectrum (Fig. 1F) of HA contained a broad, intense absorption band centered at 3421 cm^{-1}, corresponding to the O–H stretching vibration involved in intermolecular hydrogen bonding. The distinct peaks at 1617 cm^{-1} and 1408 cm^{-1} were assigned to the asymmetric and symmetric stretching vibrations of the carboxylate (C=O) groups, respectively. Meanwhile, the absorption peak at 1045 cm^{-1} was attributed to the C–O stretching vibration of primary alcohols.[28] In PSI, the absorption peak at 2955 cm^{-1} was mainly due to the C–H stretching vibrations of methylene groups (–CH_2–). Additionally, the peak at 1792 cm^{-1} resulted from the coupling of adjacent carbonyl groups, while the strong band at 1717 cm^{-1} corresponded to the C=O stretching vibration of the succinimide ring. Furthermore, the absorption peak at 1392 cm^{-1} was associated with the C–N stretching vibration within the imide ring, confirming the presence of a five-membered cyclic imide structure.[29] Importantly, the FT-IR spectrum of the synthesized HA–PSI conjugate contained new absorption bands at 1638 cm^{-1} and 1542 cm^{-1}, which are characteristic of the amide I (primarily C=O stretch) and amide II (combination of N–H bending and C–N stretching) bands, respectively. The

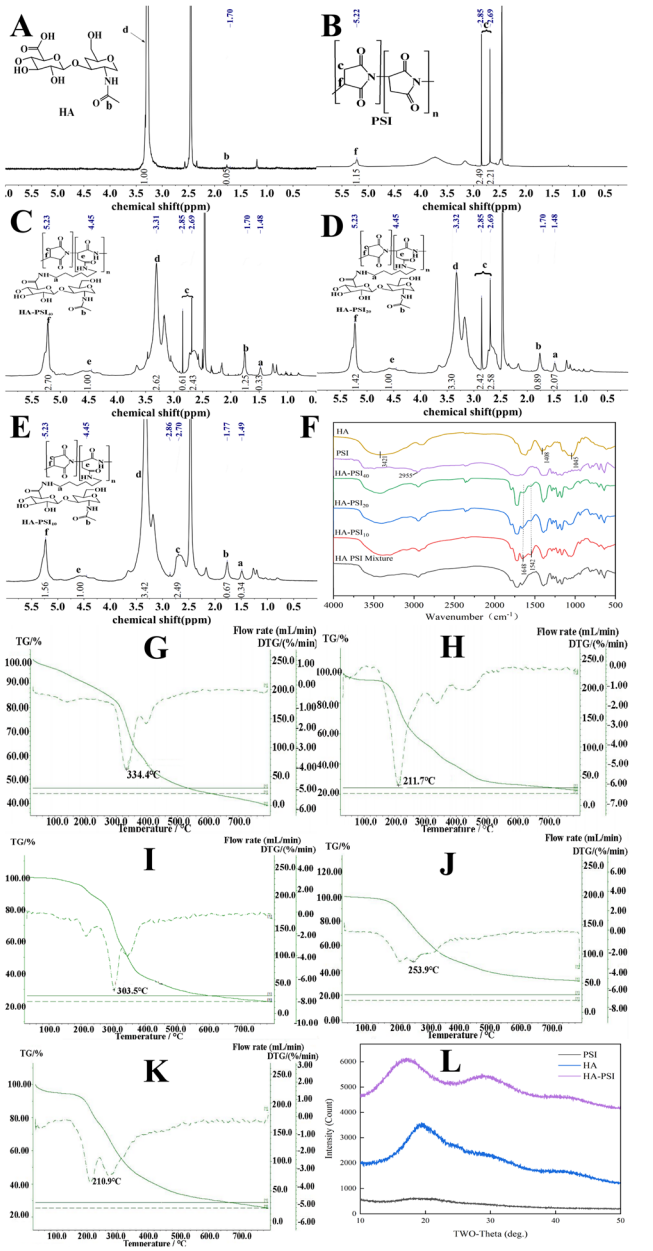

Fig. 1 Synthesis and characterization of HA, PSI, and HA–PSI conjugates. (A–E) Proton nuclear magnetic resonance (^{1}H NMR) spectra (in DMSO-d_6) of HA (A), PSI (B), HA–PSI_{40} (C), HA–PSI_{20} (D), and HA–PSI_{10} (E). (F) Fourier-transform infrared (FT-IR) spectra of HA, PSI, and the HA–PSI conjugates (HA–PSI_{40}, HA–PSI_{20}, and HA–PSI_{10}). (G–K) Thermogravimetric analysis (TGA) and derivative thermogravimetry (DTG) curves of PSI (G), HA (H), and the HA–PSI conjugates (HA–PSI_{40} [I], HA–PSI_{20} [J], and HA–PSI_{10} [K]). (L) X-ray diffraction (XRD) patterns of HA, PSI, and the HA–PSI_{40} conjugate.

emergence of these amide signals confirmed the ring-opening of PSI and its subsequent conjugation with HA.[30]

The thermal degradation behavior of the formulations was explored *via* TGA/DTG (Fig. 1G–K). PSI (Fig. 1G) exhibited three-stage decomposition behavior: an initial 8.81% weight loss below 190 °C (evaporation of free water); a major stage of weight loss between 255 °C and 385 °C (27% weight loss, dehydration

involving terminal –OH/–NH_2 groups), peaking at 334 °C; and a final step from 386 °C to 610 °C (15.16% weight loss, backbone cleavage).[19] HA (Fig. 1H) showed 4.94% weight loss below 130 °C (moisture loss), followed by rapid decomposition between 150 °C and 310 °C (42.7% weight loss), which peaked at 211.7 °C (indicative of polysaccharide chain scission). These results demonstrated the superior thermal stability of PSI over HA, which was attributable to its rigid cyclic imide structure. Interestingly, the TGA profiles of the HA–PSI conjugates (Fig. 1I–K) revealed a systematic decrease in the maximum decomposition temperature with an increase in HA content: 303.5 °C (HA–PSI_{40}), 253.9 °C (HA–PSI_{20}), and 210.9 °C (HA–PSI_{10}). This trend, approaching the degradation temperature of pure HA, could not be explained by simple physical blending or dilution effects, which typically cause peak broadening rather than a directional shift.[31] Instead, it was attributable to a nucleophilic attack by HA against the cyclic imide rings of PSI, leading to ring-opening and the conversion of the rigid cyclic structure into more flexible, linear segments. This chemical transformation lowered the activation energy required for backbone decomposition, triggering degradation at lower temperatures. In line with this, the weight losses in the 150–310 °C range for HA–PSI_{40}, HA–PSI_{20}, and HA–PSI_{10} were 33.11%, 36.83%, and 38.55%, respectively, demonstrating a positive correlation with the HA content. The distinct dual-peak profiles of the composites further provided conclusive evidence of chemical interactions rather than physical mixing. The reduced thermal stability suggested that the HA–PSI conjugates may degrade more rapidly under physiological conditions (37 °C), favorably influencing drug release kinetics.[18] Moreover, the ring-opening reaction enhanced the hydrophilicity of the system due to the generation of amide bonds and carboxylic acid groups, potentially improving swelling capacity and affecting drug loading and release profiles. This transition from a rigid cyclic to a flexible linear configuration could also potentially decrease mechanical strength while possibly increasing toughness.

The XRD patterns (Fig. 1L) showed that both PSI and HA exhibited broad, diffuse halos at $2\theta = 20.18°$ and 19.47°, respectively, which were characteristic of amorphous polymers.[32,33] The XRD pattern of the HA–PSI composite contained two new broad peaks at $2\theta = 17.05°$ and 29.25°, which differed in shape and position from those of the individual components. This reflected the molecular-level interactions between HA and PSI, leading to the rearrangement of the polymer chains and the formation of a new, homogeneous phase rather than a physical mixture. The shift in peak positions reflected the changes in interplanar spacing (d). The peak at 17.05° (larger d-spacing) was reflective of expanded interchain distances in certain regions, likely due to the insertion of polar groups from HA (*e.g.*, –COOH, –OH) between PSI or HA chains *via* hydrogen bonding.[34] Conversely, the peak at 29.25° (smaller d-spacing) indicated tighter chain packing in other regions, possibly due to chain refolding or the increased local ordering induced by interactions. The smooth, uniform amorphous halo of the composite signified the extensive and homogeneous interactions throughout the sample. Regions with reduced d-spacing could enhance the structural compactness and stability of the composite, while those with enlarged d-spacing could provide more interstitial space for drug loading and diffusion. The retained amorphous nature of the composite was advantageous for controllable dissolution/swelling behavior as a drug carrier. The XRD results confirmed that HA–PSI was an amorphous composite with a distinct, homogeneous structure formed *via* intermolecular interactions, altering the original chain packing of both polymers.

Additional characterization: the determination of the reaction time of HA–PSI is displayed in Fig. S2 (SI). The structural characterization of HAP is depicted in Fig. S3 (SI).

3.2. Optimization of the nano drug delivery system

The results of the single-factor experiments are summarized in Tables S1–S3. The optimization outcomes and corresponding analyses for each nano-formulation are provided in Tables S4 and S5, with the response surface plots shown in Fig. 2. The results demonstrated that the concentrations of both HAP and the drug (GEM) had a substantial effect on both the DLC and EE of the nano-formulations. The optimal composition of each formulation is listed in Table 1. Notably, the DLC of all nano-formulations reached approximately 30% or higher. This high loading capacity was crucial, as it could reduce the quantity of excipients required, decrease production costs, and improve the safety profile of the formulations. This advantage could be particularly valuable for formulations targeting diseases such as cancer, which often demand high-dose drug regimens.

3.3. Characterization of the nano drug delivery system

As shown in Fig. 3A–D, the final nano-formulations all exhibited a relatively uniform and near-spherical morphology. The particle sizes of GEM@(HAP/PSI), GEM@HA-$(HAP/PSI)_{40}$, GEM@HA-$(HAP/PSI)_{20}$, and GEM@HA-$(HAP/PSI)_{10}$ were found to be 133.6 nm, 159.4 nm, 170.1 nm, and 184.6 nm, respectively. Additionally, all formulations showed a low polydispersity index. The size range (approximately 100–200 nm) of the nanoparticles was within the optimal range required for exploiting the EPR effect in solid tumors and achieving passive targeting.[35] Thus, the particles could effectively circumvent the challenge of rapid renal clearance (typically affecting particles <10 nm)[36] while remaining smaller than the inter-endothelial gaps in tumor vasculature (generally 200–2000 nm), which could promote their selective accumulation at tumor sites. Moreover, their size range could minimize excessive uptake by mononuclear phagocytes in the liver and spleen (which preferentially clear particles >200 nm), prolonging systemic circulation and enhancing opportunities for drug delivery to the target tissue.[37] Meanwhile, the low polydispersity index revealed a narrow size distribution for the particles. This was reflective of the stable and reproducible preparation process, which is essential for batch-to-batch consistency and future clinical translation.[38] The zeta potential of the nanoparticles was approximately −18 mV, a moderately negative value that is consistent with the negative charge of human biological membranes.

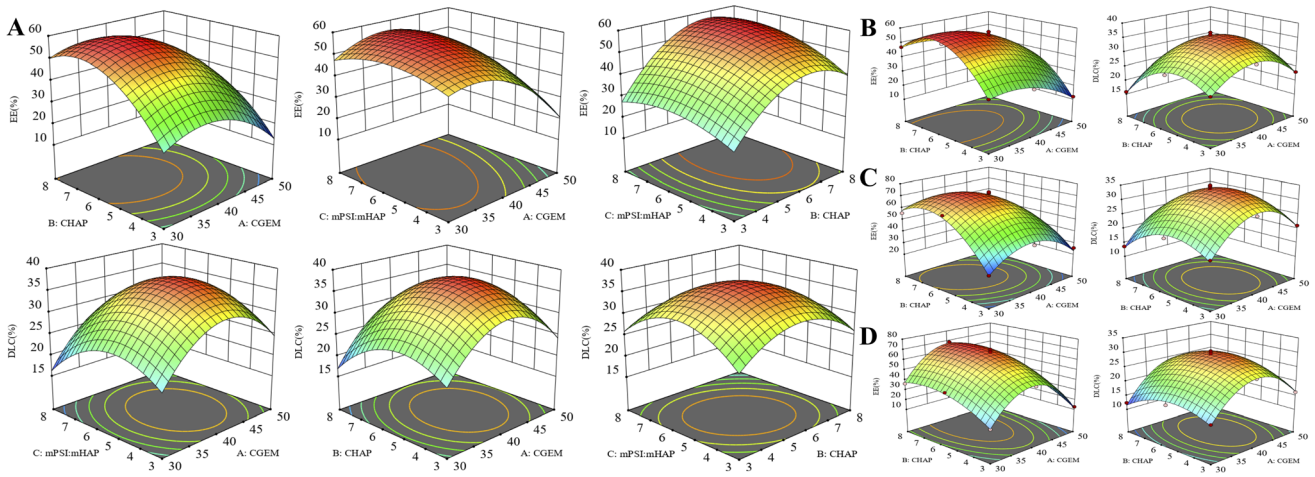

Fig. 2 Formulation optimization using three-dimensional response surface methodology. (A) GEM@(HAP/PSI); (B) GEM@HA-$(HAP/PSI)_{40}$; (C) GEM@HA-$(HAP/PSI)_{20}$; (D) GEM@HA-$(HAP/PSI)_{10}$.

Table 1 Formulation optimization results and the measured encapsulation efficiency and drug loading of the final formulation ($n = 3$)[a,b]

Nano preparations	C_{GEM} (mg mL^{-1})	C_{HAP} (mg mL^{-1})	m_{PSI} : m_{HAP}	Predicted EE (%)	Predicted DLC (%)	Measured EE (%)	Measured DLC (%)
GEM@(HAP/PSI)	39.55	5.87	5.58	56.26	36.98	56.68 ± 2.31	37.07 ± 0.60
GEM@HA-$(HAP/PSI)_{40}$	38.60	5.57	6.00	56.02	35.11	56.63 ± 1.03	34.95 ± 1.19
GEM@HA-$(HAP/PSI)_{20}$	39.39	5.67	8.00	70.55	33.26	71.93 ± 0.14	34.21 ± 0.24
GEM@HA-$(HAP/PSI)_{10}$	40.45	5.99	10.00	68.31	29.07	72.73 ± 2.86	30.14 ± 0.74

[a] Abbreviations: *C*, concentration; GEM, gemcitabine; HA, hyaluronic acid; PSI, polysuccinimide; HAP, hydroxyapatite; EE, encapsulation efficiency; DLC, drug loading capacity. [b] $EE = M_1 \times 100/M_0$ and $DLC = M_1 \times 100/(M_1 + M_2)$. M_1 is the mass of the drug in the carrier, M_0 is the total mass of the added drug, and M_2 is the total mass of the blank carrier, GEM standard curve was shown in Fig. S1.

The *in vitro* drug release profiles of the different formulations under various pH conditions (5.0, 6.8, and 7.4) are presented in Fig. 3E. After 24 h, the cumulative drug release from GEM@(HAP/PSI) reached approximately 41%, 58%, and 60% at pH 5.0, 6.8, and 7.4, respectively. Following HA modification, the drug release rates increased for GEM@HA-$(HAP/PSI)_{40}$, GEM@HA-$(HAP/PSI)_{20}$, and GEM@HA-$(HAP/PSI)_{10}$, with 24-h releases of 64%, 69%, and 79% at pH 7.4; 62%, 66%, and 75% at pH 6.8; and 43%, 47%, and 49% at pH 5.0, respectively. All formulations exhibited clear pH-dependent release properties, showing markedly slower and incomplete release at pH 5.0. Interestingly, GEM@HA-$(HAP/PSI)_{10}$ initially showed a slower release rate than GEM@HA-$(HAP/PSI)_{20}$ within the first 12 h, but its release rate surpassed that of all other formulations thereafter. This biphasic pattern could be attributed to the dense HA brush on the surface of GEM@HA-$(HAP/PSI)_{10}$. Initially, the hydrated HA layer impeded water penetration, preventing drug release. However, after water penetrated the barrier, the higher HA content promoted the more rapid degradation of the PSI matrix, accelerating drug release at later stages.

The accelerated and more complete drug release observed at pH 7.4 was attributed to the presence of abundant succinimide rings (five-membered cyclic anhydrides) within the PSI backbone, which are highly susceptible to hydrolysis under alkaline conditions.[39] The high concentration of strongly nucleophilic hydroxide ions (OH^-) under these pH conditions facilitated the efficient attack and cleavage of these rings, leading to the rapid hydrolysis of the polymer backbone, subsequent nanoparticle disassembly, and faster drug release. In contrast, under acidic conditions, the high concentration of H^+ and the limited availability of OH^- restricted hydrolysis, which was then mediated primarily *via* water molecules (H_2O). Given the relatively weaker nucleophilicity of water, the hydrolysis of succinimide rings was significantly slower, allowing the nanoparticles to retain greater structural integrity. This resulted in more sustained and slower drug release.

Although the extracellular microenvironment of most solid tumors is weakly acidic (pH ~6.5–7.0), the intracellular pH of tumor cells is near-neutral to slightly alkaline (approximately 7.2–7.4), comparable to or slightly higher than that of normal cells.[40] Thus, for therapeutics that act within the cytoplasm or nucleus (*e.g.*, DNA-damaging agents such as GEM), delivery systems capable of rapid drug release at pH 7.4 are advantageous. Such systems promote efficient intracellular drug unloading after cellular uptake, thereby enhancing cytotoxic efficacy. This proposed release mechanism is consistent with typical intracellular trafficking pathways. After endocytosis, nanoparticles are encapsulated within endosomes. As these vesicles mature and fuse with lysosomes, their intraluminal pH

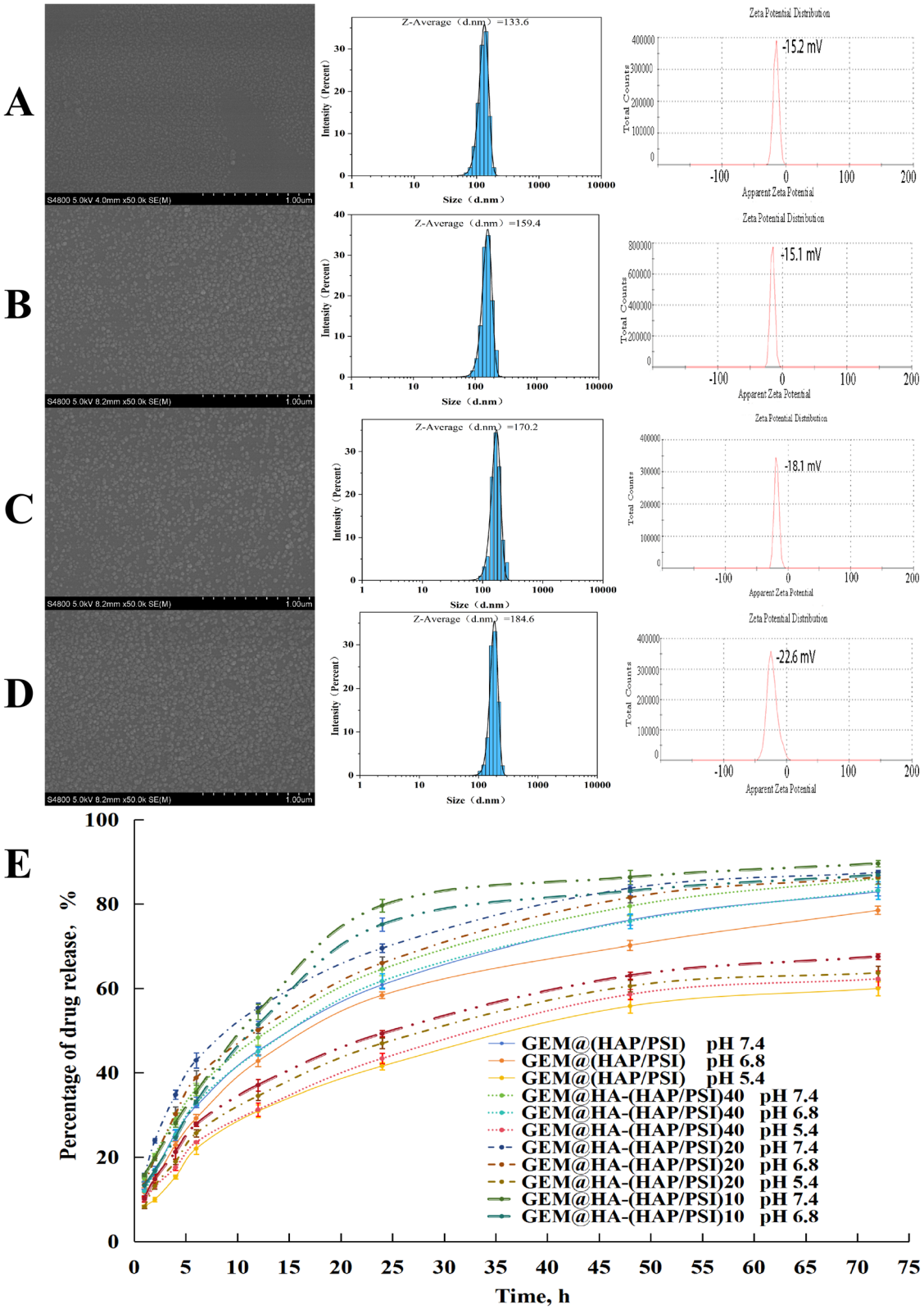

Fig. 3 Physicochemical characterization and *in vitro* drug release profiles of the various nano-formulations. (A–D) Representative scanning electron microscopy (SEM) images, particle size distribution (PSD), and zeta potential of the different formulations: (A) GEM@(HAP/PSI); (B) GEM@HA-$(HAP/PSI)_{40}$; (C) GEM@HA-$(HAP/PSI)_{20}$; (D) GEM@HA-$(HAP/PSI)_{10}$. (E) *In vitro* drug release profiles of the formulations under different pH conditions.

decreases from approximately 6.5 to 5.0. The stability of PSI-based carriers under these acidic endo-lysosomal conditions helps protect the encapsulated drug from premature degradation. Subsequently, when the nanoparticles escape the endo-lysosomal compartment or are exposed to the near-neutral cytosolic pH (~7.4), they undergo rapid disintegration, triggering a burst release of the drug into the cytoplasm. This pH-triggered release mechanism is particularly beneficial for the delivery of macromolecular therapeutics (*e.g.*, nucleic acids and proteins), which are vulnerable to lysosomal degradation and require efficient cytosolic release to exert their biological action.

The drug release profiles of the formulations were fitted to various kinetic models, including the zero-order, first-order, Higuchi, and Korsmeyer–Peppas models. As shown in Table 2, the Korsmeyer–Peppas model exhibited the highest correlation coefficients (R^2) for most formulation groups. One exception was GEM@HA-(HAP/PSI)$_{10}$ at pH 6.8 and 7.4, where the first-order model provided a marginally better fit. The release exponent (n) obtained from the Korsmeyer–Peppas model was consistently below 0.4 for all formulations, unequivocally indicating a drug-release mechanism dominated by Fickian diffusion. The uniformity of this mechanism across the tested pH range suggested that pH variation did not induce fundamental changes in carrier structure, such as significant polymer erosion or matrix disintegration.

Notably, the Fickian diffusion-controlled process ($n < 0.45$) implied that the release rate of the formulations was primarily governed by the concentration gradient of the drug within the carrier matrix, with molecules diffusing outward *via* pores or aqueous channels. The low n values effectively precluded the possibility of mechanisms governed by polymer chain relaxation or swelling (Case-II or anomalous transport).[41] Overall, the diffusion-dominated profile appeared to be advantageous, as it typically provides more gradual and predictable release kinetics, thereby minimizing the risk of an initial burst release, which is associated with rapid carrier degradation.[42] Such controlled release is often critical for maintaining stable therapeutic drug levels and mitigating toxicity. In this study, the nanocarrier demonstrated robust physical and chemical stability across the physiological pH spectrum (5.0–7.4), functioning as a stable reservoir without undergoing rapid dissolution. This property could enable sustained drug delivery over an extended period, prolonging therapeutic effects and potentially improving patient compliance by reducing the dosing frequency. For GEM, a prodrug requiring intracellular activation *via* phosphorylation,[23] a sustained release profile could help maintain effective concentrations of the corresponding active metabolites, potentially countering certain metabolism-related resistance mechanisms. The consistent observation of Fickian diffusion as the primary release mechanism across different formulations indicated that the core release behavior of the nanocarriers was robust and largely insensitive to preparation parameters, such as the HA content. These features could be favorable for future scale-up and quality control.

In summary, the nanoplatform prepared in this study exhibited an ideal, diffusion-controlled release profile. Its stable structure could facilitate sustained release by modulating diffusion rates while preventing structural collapse. Notably, the release exponent (n) tended to decrease with an increase in HA modification. The denser HA hydration layer could initially act as a diffusion barrier, moderating the initial release phase. Subsequent water penetration likely altered the swelling and permeability of the polymer matrix, thereby reinforcing diffusion-dominated characteristics in later stages. Specifically for the GEM@HA-(HAP/PSI)$_{10}$ formulation, release at pH 7.4 and 6.8 followed first-order kinetics, which are often characteristic of diffusion-controlled processes where the release rate is proportional to the remaining drug load. These findings reflected the relative structural stability of the carrier within this pH range, with minimal contribution from polymer swelling or degradation. The slightly higher n values at pH 7.4 and 6.8 for the high-HA-content formulation could indicate the presence of minor matrix erosion processes. Nevertheless, the First-order kinetics at neutral pH implied predictable release behavior, which is beneficial for stability during systemic circulation. Meanwhile, the Fickian behavior ($n < 0.45$) under acidic pH

Table 2 Fitting parameters of the drug release kinetics models of the different formulations[a]

		R^2				
Preparations	Medium	Zero-order	First-order	Higuchi	Korsmeyer-Peppas	n
GEM@(HAP/PSI)	pH7.4	0.8455	0.9615	0.9676	0.9814	0.4037
	pH6.8	0.8391	0.9712	0.9636	0.9766	0.4127
	pH5.0	0.8630	0.9719	0.9737	0.9803	0.4423
GEM@HA-(HAP/PSI)$_{40}$	pH7.4	0.8373	0.9444	0.9642	0.9834	0.3768
	pH6.8	0.8381	0.9668	0.9643	0.9788	0.4060
	pH5.0	0.8760	0.9507	0.9790	0.9865	0.4224
GEM@HA-(HAP/PSI)$_{20}$	pH7.4	0.7727	0.9440	0.9280	0.9661	0.3364
	pH6.8	0.8071	0.9555	0.9480	0.9726	0.3732
	pH5.0	0.8318	0.9690	0.9607	0.9748	0.4112
GEM@HA-(HAP/PSI)$_{10}$	pH7.4	0.7430	0.9793	0.9029	0.9294	0.3801
	pH6.8	0.7556	0.9882	0.9117	0.9324	0.4014
	pH5.0	0.8419	0.9551	0.9662	0.9818	0.3966

[a] Abbreviations: GEM, gemcitabine; HA, hyaluronic acid; PSI, polysuccinimide; HAP, hydroxyapatite.

conditions confirmed the structural integrity of the nanocarriers and the absence of excessive swelling, supporting their suitability for intracellular delivery. Finally, the high correlation coefficients (R^2 > 0.94) for both the first-order and Higuchi models across all nano-formulations also corroborated the diffusion-dominated release mechanism, as these models are widely used to describe diffusion-controlled systems.

3.4. Biocompatibility and cytotoxicity assessment

Results from the *in vitro* hemolysis assays are shown in Fig. 4A–D. Following co-incubation, the supernatants of the GEM@(HAP/PSI), GEM@HA-(HAP/PSI)$_{40}$, GEM@HA-(HAP/PSI)$_{20}$, and GEM@HA-(HAP/PSI)$_{10}$ group samples appeared clear and nearly colorless, with obvious red blood cell (RBC) sedimentation at the bottom of the tubes. The profile of these samples was indistinguishable from that of the negative control and clearly distinct from the hemolyzed positive control. As shown in Fig. 4E, the hemolysis rates in all formulation groups remained below 2%, confirming the excellent hemocompatibility of the formulations.[43] This indicated that the nanoparticles did not disrupt the integrity of the erythrocyte membranes under the tested conditions. Typically, hemolysis is induced by factors such as surface activity, hydrophobicity, sharp edges, or strong positive charges on nanomaterials, which can lead to membrane rupture. The observed biocompatibility of the nanoparticles was consistent with their moderately negative zeta potential (≈−18 mV), which likely reduced electrostatic adsorption to the negatively charged RBC membrane and prevented any physical stress or osmotic imbalance due to nanoparticle aggregation.[44] These results demonstrated that, within the tested concentration range, the formulations had a minimal impact on RBCs and presented a low risk of hemolysis, providing a reliable safety foundation for subsequent analyses.

As shown in Fig. 4F and G, the cell viabilities of both A549 and H358 cells treated with gradient concentrations of the blank carriers—(HAP/PSI), HA-(HAP/PSI)$_{40}$, HA-(HAP/PSI)$_{20}$, and HA-(HAP/PSI)$_{10}$—consistently exceeded 85%. This indicated that the nanocarriers possessed good biocompatibility and exhibited no intrinsic cytotoxicity toward either cell line, producing negligible effects on cell growth and metabolism. The primarily non-toxic nature of the blank carriers ensured that any antitumor effects observed in subsequent experiments could confidently be attributed to the released GEM rather than to the nonspecific cytotoxicity of the carrier material. Furthermore, carriers with varying degrees of HA modification also showed low toxicity, confirming that the HA conjugation process was safe and did not introduce unexpected cytotoxicity. Given the inherent safety of the carriers, the inhibitory effects of

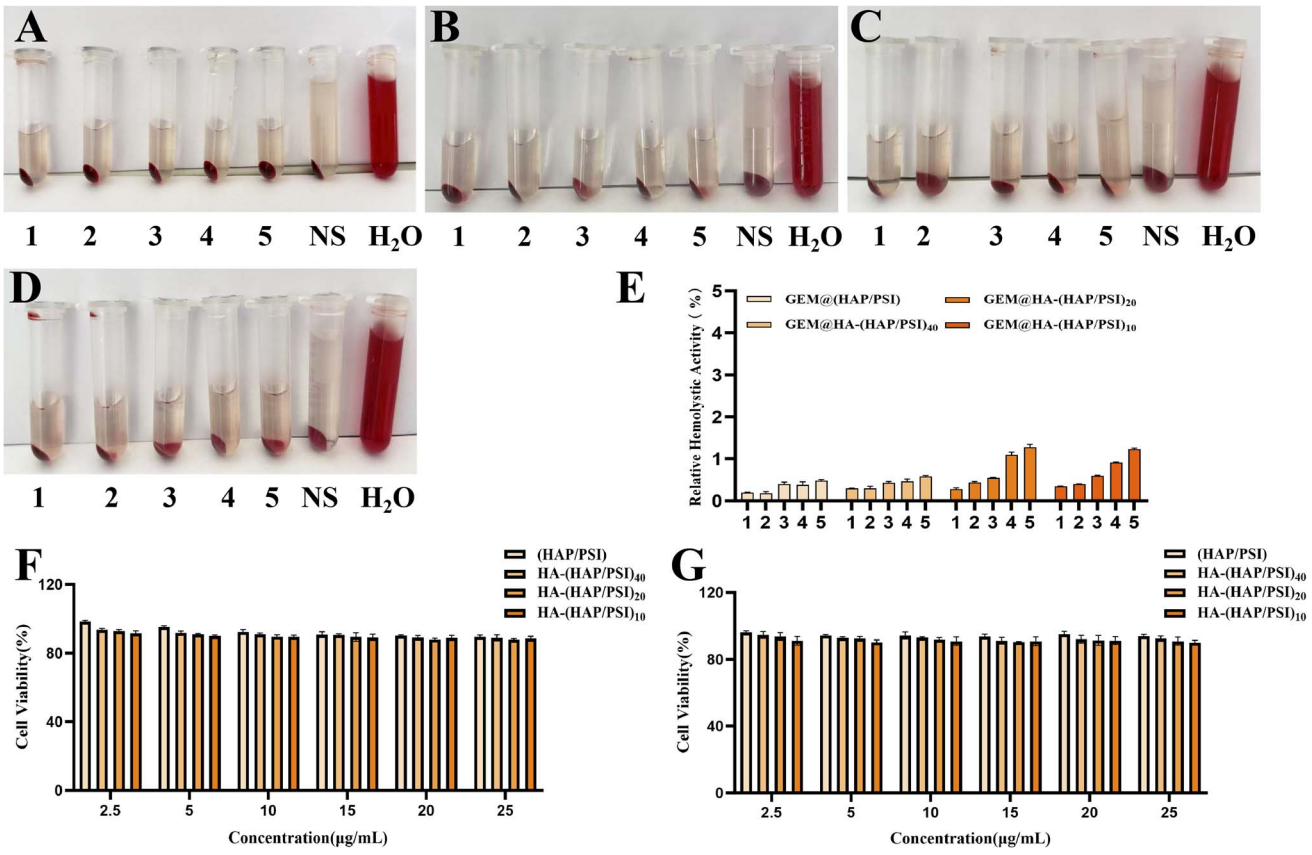

Fig. 4 Hemocompatibility and *in vitro* safety of the nano-formulations. (A–D) Representative images of erythrocytes incubated with (A) GEM@(HAP/PSI), (B) GEM@HA-(HAP/PSI)$_{40}$, (C) GEM@HA-(HAP/PSI)$_{20}$, and (D) GEM@HA-(HAP/PSI)$_{10}$. (E) Quantification of hemolysis rates. *In vitro* cytotoxicity of blank carriers against (F) A549 and (G) H358 cells, assessed using cell viability assays.

the drug-loaded formulations would more accurately reflect the delivery efficiency and therapeutic activity of GEM, thereby ensuring the reliability and interpretability of subsequent cell-based experiments. Moreover, the excellent hemocompatibility and low cytotoxicity collectively demonstrated that these nanoparticles were unlikely to provoke significant acute inflammatory responses or induce toxicity against normal tissues upon systemic administration.

3.5. Investigation into the mechanisms of cellular internalization

The *in vitro* antiproliferative effects of free GEM and the nano-formulations GEM@(HAP/PSI), GEM@HA-$(HAP/PSI)_{40}$, GEM@HA-$(HAP/PSI)_{20}$, and GEM@HA-$(HAP/PSI)_{10}$ were first evaluated using the CCK-8 assay. As shown in Fig. 5A and B, the cell viability in both cell lines decreased with increasing GEM

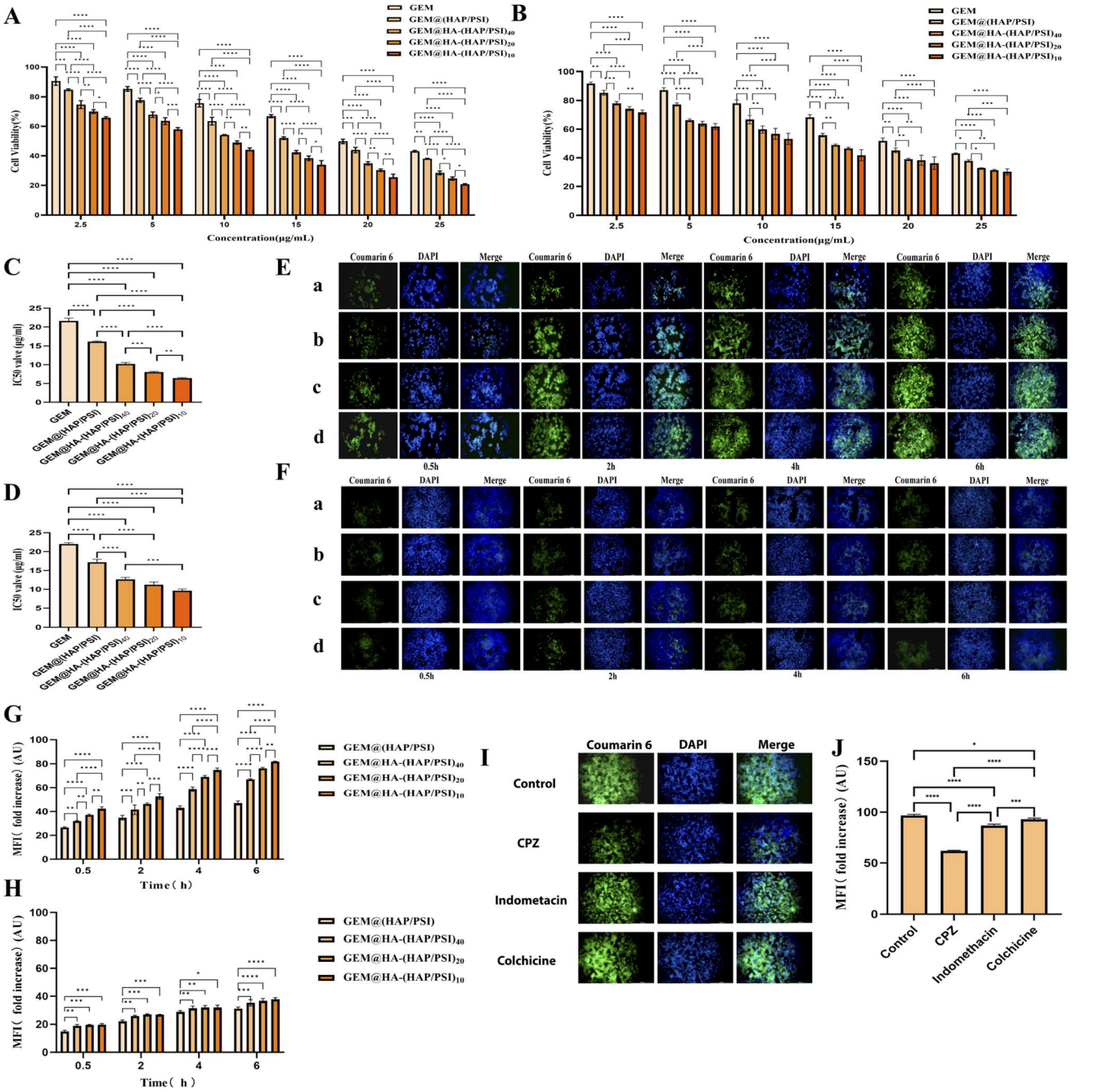

Fig. 5 *In vitro* cytotoxicity, cellular uptake, and internalization mechanisms. (A and B) Cell viability of (A) A549 and (B) H358 cells treated with increasing concentrations of the nano-formulations. (C and D) Half-maximal inhibitory concentration (IC_{50}) values of the formulations for (C) A549 and (D) H358 cells. (E and F) Representative fluorescence microscopy images showing cellular uptake in (E) A549 and (F) H358 cells. (G and H) Quantification of cellular uptake, detected based on mean fluorescence intensity (MFI), in (G) A549 and (H) H358 cells. (I and J) Investigation of the uptake mechanisms in A549 cells. (a) GEM@(HAP/PSI); (b) GEM@HA-$(HAP/PSI)_{40}$; (c) GEM@HA-$(HAP/PSI)_{20}$; (d) GEM@HA-$(HAP/PSI)_{10}$. Data are presented as the mean ± standard deviation ($n \geq 3$). *$p < 0.05$, **$p < 0.01$, ***$p < 0.001$, ****$p < 0.0001$.

concentration, in a dose-dependent manner. Moreover, all nano-formulations provided stronger growth inhibition than free GEM, with the HA-modified variants (GEM@HA-(HAP/PSI)$_{40/20/10}$) yielding slightly greater potency than the non-targeted variant GEM@(HAP/PSI).

The half-maximal inhibitory concentration (IC_{50}) values are summarized in Fig. 5C and D. After 24 h of treatment, in A549 cells, the IC_{50} values for free GEM, GEM@(HAP/PSI), GEM@HA-(HAP/PSI)$_{40}$, GEM@HA-(HAP/PSI)$_{20}$, and GEM@HA-(HAP/PSI)$_{10}$ were 21.59, 16.08, 10.19, 8.03, and 6.24 μg mL^{-1}, respectively. Meanwhile, the corresponding values in H358 cells were 22.01, 17.19, 12.62, 11.21, and 9.63 μg mL^{-1}. These results demonstrated that all drug-loaded nanoparticles displayed lower IC_{50} values than free GEM, confirming that the nano-delivery system significantly enhanced the cytotoxic effects of GEM against lung cancer cells. This enhancement could be attributed to the more efficient cellular internalization of the nanocarriers *via* endocytosis, the protection of GEM from extracellular degradation, and sustained intracellular release, which collectively increased and maintained effective drug concentrations. For A549 cells, the IC_{50} value decreased progressively with increasing HA concentrations, indicating that drug efficacy was positively correlated with the density of HA modification. This suggested that a higher surface density of HA ligands could promote stronger, potentially multivalent interactions with CD44 receptors, leading to more efficient receptor-mediated uptake. These findings were consistent with the results of TGA and XRD analysis, which revealed an increase in chemical modification and cross-linking following higher HA incorporation, potentially optimizing intracellular drug-release kinetics. For formulations with the same HA modification level, the IC_{50} values were consistently lower in A549 cells than in H358 cells. This not only reflected the higher CD44 expression in A549 cells but also directly demonstrated that the cytotoxicity of HA-modified nanoparticles was dependent on CD44 receptor-mediated pathways. Nevertheless, even in H358 cells, which express low levels of CD44, the HA-modified formulations still showed lower IC_{50} values than the non-targeted formulations. This residual activity could arise from a combination of low-level receptor interactions and passive targeting effects, with variations among HA-modified groups potentially attributable to differences in drug-release profiles.

To visualize the cellular uptake of the nanomedicines, C6 was employed as a fluorescent probe and incorporated into the nanoparticles. As shown in Fig. 5E and F, C6-labeled nanoparticles emitted green fluorescence, while nuclei appeared blue due to DAPI counterstaining. In CD44-high A549 cells (Fig. 5E and G), a faint green signal was detectable in all groups at 0.5 h, indicating the initial cellular entry of the nano-formulations. Thereafter, the fluorescence intensity increased markedly at 2 h, reflecting enhanced internalization. Moreover, the fluorescence intensity peaked at 4 h and remained strong even at 6 h, without obvious attenuation. This time-dependent increase in fluorescence across all formulations was indicative of progressive cellular accumulation rather than mere surface adsorption. The sustained signal at 6 h revealed the effective intracellular retention of the nanoparticles, which was favorable for prolonged drug release. Notably, the fluorescence intensity of HA-modified nanoparticles (HA-(HAP/PSI)$_{40}$, HA-(HAP/PSI)$_{20}$, and HA-(HAP/PSI)$_{10}$) remained consistently higher than that of the non-targeted (HAP/PSI) formulation. Moreover, the signal intensity was positively correlated with the density of HA modification (Fig. 5G), implying that a higher surface density of HA ligands led to greater cellular internalization. This visual evidence directly supported the active targeting functions of HA and aligned well with the enhanced cytotoxic efficacy observed in the CCK-8 assay, indicating that HA-(HAP/PSI)$_{10}$ possessed the most efficient targeting and delivery profile. In contrast, in CD44-low H358 cells (Fig. 5F and H), the fluorescence signals were generally weak at all time points. Although the HA-modified formulations exhibited slightly higher fluorescence intensity than the unmodified control, the difference was marginal, and no significant difference was observed among the different HA-modified groups. This stark contrast to the uptake pattern in A549 cells indicated that the beneficial effects of HA modification are highly dependent on CD44 receptor expression. In summary, the findings showed that HA modification significantly enhances nanoparticle uptake in target cells (A549) in a time- and dose (HA ratio)-dependent manner, primarily *via* CD44 receptor-mediated pathways. The pronounced enhancement of fluorescence in CD44-high A549 cells, coupled with its minimal effect in CD44-low H358 cells, confirmed the targeting specificity and receptor-driven mechanism of the designed nanocarrier system.

Building on the cellular uptake observations, we further explored the endocytic mechanisms of the lead formulation, GEM@HA-(HAP/PSI)$_{10}$, in A549 cells. Non-viral nanocarriers typically enter cells *via* endocytosis and are internalized within vesicles that subsequently mature into endosomes. Mammalian cells possess several distinct endocytic pathways, including clathrin-mediated endocytosis (CME), caveolin-mediated endocytosis, macropinocytosis, and clathrin-/caveolin-independent mechanisms.[45] The specific route and efficiency of nanoparticle uptake are influenced by multiple factors, including particle size, surface charge, material composition, and surface ligands. Often, internalization occurs through a combination of pathways rather than a single route. Thus, to delineate the primary uptake mechanism, A549 cells were pretreated with specific pharmacological inhibitors prior to incubation with C6-labeled nanoparticles.

As shown in Fig. 5I and J, the cellular uptake of the nanoparticles was significantly inhibited by chlorpromazine (CME inhibitor), decreasing to 62.06% of control levels. This substantial reduction (~38% inhibition) indicated that CME was the predominant pathway for GEM@HA-(HAP/PSI)$_{10}$ uptake in these cells. In the CME route, cargo is typically trafficked to lysosomes *via* early and late endosomes.[46] In this scenario, the slow drug release profile of our nanocarrier under acidic lysosomal pH could protect the payload from enzymatic degradation, offering potential advantages for the delivery of labile therapeutics such as nucleic acids. Notably, the cellular uptake of the nano-formulations was also partially inhibited by indomethacin (caveolin-mediated endocytosis inhibitor), decreasing to 86.56% of control levels (~13% inhibition), reflecting a contributory role for this pathway as well. Caveolin-

mediated endocytosis often bypasses lysosomal degradation, potentially directing cargo to alternative intracellular compartments such as the Golgi apparatus or endoplasmic reticulum.[47] Finally, a minor reduction to 93.02% of control levels (~7% inhibition) was observed after colchicine (macropinocytosis inhibitor) treatment, suggesting a limited role for this non-specific fluid-phase uptake mechanism. In summary, our results indicated that GEM@HA-$(HAP/PSI)_{10}$ nanoparticles enter A549 cells primarily *via* CME, with caveolin-mediated endocytosis and macropinocytosis acting as secondary pathways. Such engagement of multiple entry mechanisms could be advantageous, potentially reducing the likelihood of cellular resistance due to the circumvention of any single uptake route.[48]

3.6. Antitumor efficacy *in vitro*

As shown in Fig. 6A, A549 cells in the blank control group displayed a typical polygonal morphology and remained well-adhered and viable. In comparison, the cells treated with free GEM showed only modest morphological changes, largely retaining their structural integrity. By contrast, marked alterations were detected in cells treated with GEM@(HAP/PSI), GEM@HA-$(HAP/PSI)_{40}$, GEM@HA-$(HAP/PSI)_{20}$, and GEM@HA-$(HAP/PSI)_{10}$. These cells exhibited obvious shrinkage, a loss of the original polygonal shape, and a pronounced decrease in cell density.

The migratory capacity of A549 cells was evaluated using a scratch assay. Following wound induction in a cell monolayer, the cells were treated with various formulations, and wound closure was monitored at 0, 12, and 24 h (Fig. 6B). In the control group, extensive wound closure was observed by 24 h, with a healing rate of 53.86%. In contrast, cell migration was significantly suppressed in all nano-formulation-treated groups. Notably, the GEM@(HAP/PSI) group showed markedly reduced migration when compared to the control group. However, the HA-modified formulations—GEM@HA-(HAP/

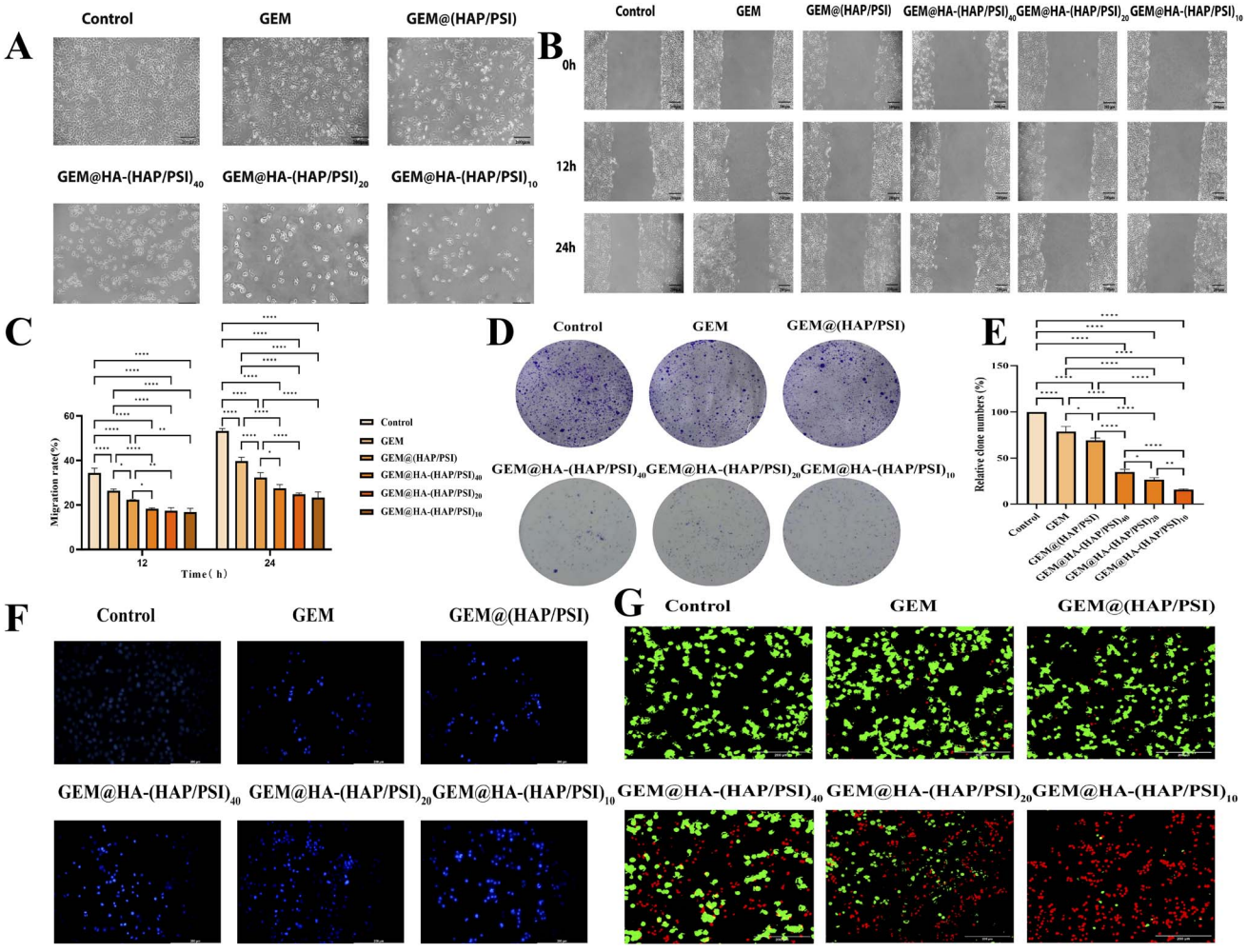

Fig. 6 *In vitro* antitumor efficacy in A549 cells. (A) Representative bright-field images showing morphological changes in A549 cells after treatment. (B) Wound healing (scratch) assay at 0, 12, and 24 h. (C) Quantitative analysis of cell migration rates at 12 h and 24 h. (D) Colony formation assay. (E) Quantitative analysis of colony numbers. (F) Nuclear morphology assessed *via* Hoechst 33 342 staining. (G) Cell viability assessed *via* Calcein-AM/PI (live/dead) staining. Data are presented as the mean ± standard ($n \geq 3$). *$p < 0.05$, **$p < 0.01$, ***$p < 0.001$, ****$p < 0.0001$.

$PSI)_{40}$, GEM@HA-$(HAP/PSI)_{20}$, and GEM@HA-$(HAP/PSI)_{10}$—yielded even stronger inhibition of cell migrations, leading to 24-h migration rates below 30% (Fig. 6C). At both 12 h and 24 h, the migration rates in these HA-modified groups were significantly lower than those in the non-targeted GEM@(HAP/PSI) group. These results indicated that all nano-formulations can effectively inhibit cell migration, with their anti-migratory effect positively correlating with the extent of HA modification. This enhancement could be attributed to the specific binding of HA to overexpressed CD44 receptors on the cell surface, promoting the greater cellular internalization of the nanoparticles. The higher intracellular drug accumulation could lead to a more effective disruption of migration-associated signaling pathways, leading to a superior inhibition of cell migration.[49]

The colony-forming capacity of A549 cells was also assessed following treatment with different formulations. From a morphological perspective, numerous regularly shaped colonies were detected in the control group, indicating robust proliferative capacity (Fig. 6D). In contrast, both the free GEM and GEM@(HAP/PSI) groups exhibited irregular colony morphology, loosely arranged cells, heterogeneous colony sizes, and a marked reduction in colony number. As expected, the HA-modified nano-formulations induced an even stronger suppression of clonogenicity (Fig. 6E). While free GEM reduced colony formation to 73.93% of control levels, nano-encapsulation alone (GEM@(HAP/PSI)) further lowered it to 64.02%, indicating that the carrier could itself enhance the anti-proliferative effect. This inhibition was significantly intensified upon HA modification, with colony formation decreasing sharply from 36.68% in the GEM@HA-$(HAP/PSI)_{40}$ group to 17.16% in the GEM@HA-$(HAP/PSI)_{10}$ group. This dose-dependent enhancement suggested that a higher density of HA surface ligands can promote more efficient receptor clustering and internalization. This leads to greater intracellular drug accumulation and a consequently stronger inhibitory effect on tumor stemness and proliferation-related pathways.

Apoptosis was evaluated in A549 cells following drug treatment using Hoechst staining. As shown in Fig. 6F, the nuclei in the control group displayed intact morphology and structure, exhibiting faint blue fluorescence. In contrast, the GEM@(HAP/PSI) group showed nuclear shrinkage, the loss of membrane integrity, and bright blue fluorescence. Compared with the free GEM group, the GEM@HA-$(HAP/PSI)_{40}$, GEM@HA-$(HAP/PSI)_{20}$, and GEM@HA-$(HAP/PSI)_{10}$ groups all exhibited a marked increase in apoptotic cell counts, characterized by enhanced nuclear staining and more intense fluorescence—the hallmarks of late apoptosis (chromatin condensation and nuclear fragmentation). The number of apoptotic cells was significantly higher in the HA-modified groups than in the non-HA-modified group, further suggesting that increasing intracellular drug concentrations *via* targeted internalization leads to the more effective activation of mitochondrial- or death receptor-mediated apoptotic pathways.[50]

Subsequently, cell viability was evaluated using a double-staining assay with Calcein-AM and PI. Calcein-AM is a non-fluorescent dye that is hydrolyzed by intracellular esterases in live cells to produce green-fluorescent Calcein, which is retained within cells that have intact membranes. PI, on the other hand, is membrane-impermeable and only enters cells with compromised membranes, intercalating into DNA molecules and emitting red fluorescence. Thus, live cells fluoresce green, whereas dead cells fluoresce red, allowing for the assessment of nanoparticle-induced cytotoxicity. As shown in Fig. 6G, compared with the control group, the free GEM and GEM@(HAP/PSI) groups exhibited faint red fluorescence. In contrast, the GEM@HA-$(HAP/PSI)_{40}$, GEM@HA-$(HAP/PSI)_{20}$, and GEM@HA-$(HAP/PSI)_{10}$ groups showed a pronounced increase in red fluorescence, accompanied by a concomitant decrease in green fluorescence. These findings aligned with the results of the colony formation assay, indicating that HA-modified nanoparticles not only inhibit proliferation but also induce extensive cell death. The enhanced cytotoxic effect likely stemmed from the CD44-mediated endocytosis of the nanoparticles, which could thereby bypass certain efflux pumps, allowing the drug to reach the intracellular threshold concentration required to more efficiently trigger apoptosis or necrosis.[51]

Based on the comprehensive experimental evidence, we inferred that the efficacy of the various formulations followed the following order: GEM@HA-$(HAP/PSI)_{10}$ > GEM@HA-$(HAP/PSI)_{20}$ > GEM@HA-$(HAP/PSI)_{40}$ > GEM@(HAP/PSI) > free GEM > control. This observed hierarchy could be attributed to the distinct delivery and action mechanisms of each formulation. The limited efficacy of free GEM was likely due to its reliance on passive diffusion, which is inefficient and susceptible to efflux pump activity. In contrast, the GEM@(HAP/PSI) nanocarrier could enhance therapeutic outcomes by improving cellular uptake—presumably *via* the EPR effect *in vivo* or general endocytosis *in vitro*—while simultaneously enabling sustained drug release and protection from degradation. In this scenario, the incorporation of HA as a targeting ligand provided a significant advancement. The specific binding of HA to overexpressed CD44 receptors on A549 cells triggered highly efficient, receptor-mediated active endocytosis pathways (primarily *via* clathrin-dependent mechanisms). This facilitated the targeted enrichment and intracellular delivery of GEM-loaded nanoparticles, leading to a drastic increase in intracellular drug concentration. As a result, superior therapeutic effects were observed across multiple cellular processes, including the inhibition of migration and proliferation, as well as the induction of apoptosis. Beyond their role as delivery carriers, the nanoparticles could enable the HA–CD44 interaction, which itself may modulate the malignant phenotype of tumor cells. Since CD44 is a key signaling molecule associated with the regulation of cell migration, proliferation, and survival, its persistent engagement by HA-conjugated nanoparticles could competitively inhibit the interaction between endogenous HA and CD44, thereby disrupting downstream pro-oncogenic signaling cascades (*e.g.*, PI3K/Akt, Ras/MAPK). This modulatory effect may act synergistically with the direct cytotoxic action of GEM.

In summary, our *in vitro* pharmacodynamic analyses demonstrated that GEM@HA-$(HAP/PSI)_{10}$ exhibits potent and multifaceted abilities to inhibit A549 cell migration and

proliferation and to induce cell death, outperforming both the non-targeted nanocarrier and free GEM.

3.7. *In vivo* antitumor activity and pharmacodynamic evaluation

Based on our *in vitro* pharmacodynamic findings, we further evaluated the *in vivo* antitumor efficacy of GEM@HA-(HAP/PSI)$_{10}$ in a xenograft mouse model. A commercially available GEM formulation (Eli Lilly and Company) and saline were used as the positive and negative controls, respectively. As shown in Fig. 7A and B, after 15 days of treatment, both the commercial GEM and GEM@HA-(HAP/PSI)$_{10}$ groups exhibited significantly smaller tumor volumes than the saline control group, indicating the effective suppression of tumor growth. Notably,

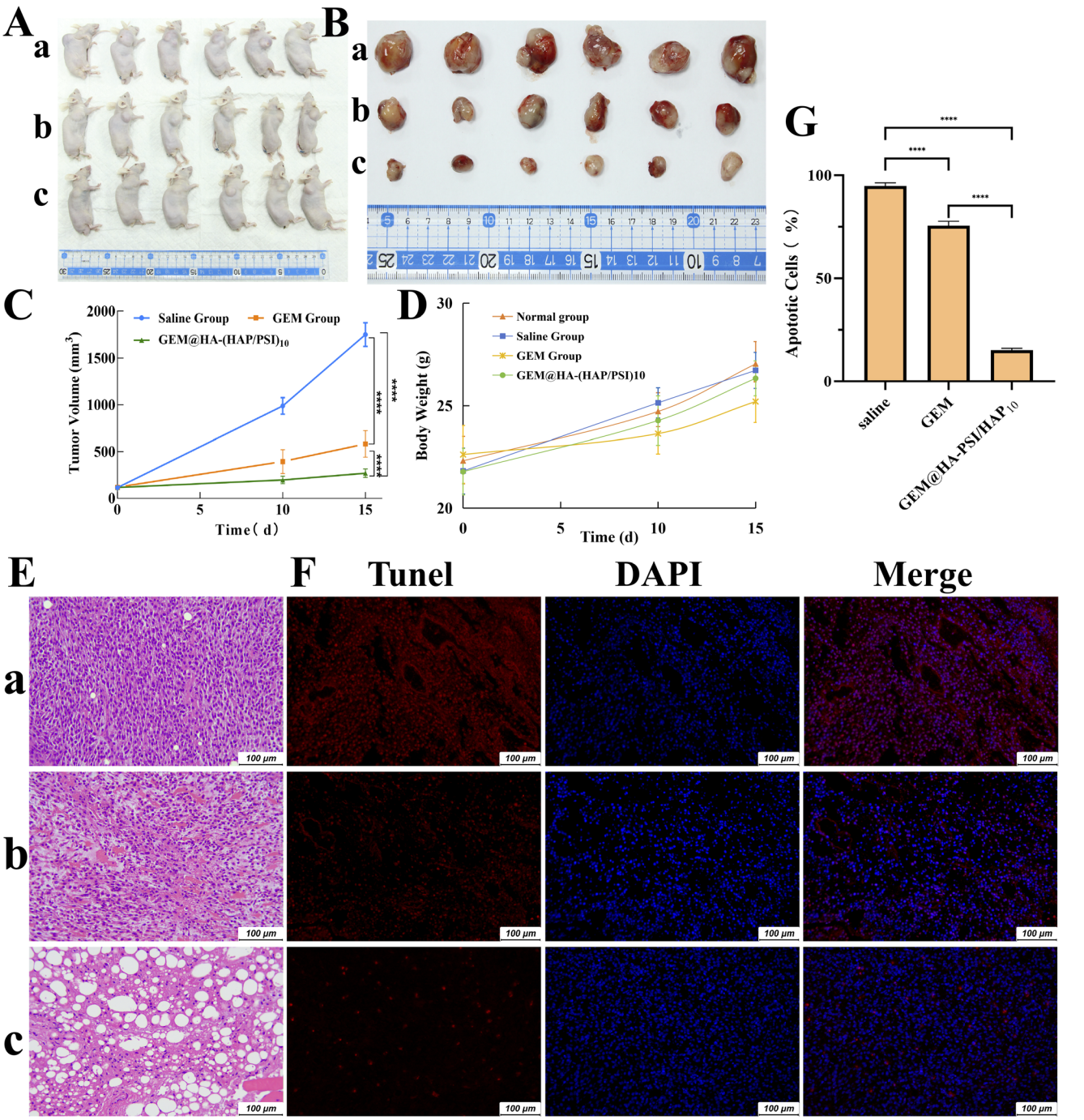

Fig. 7 *In vivo* antitumor efficacy in a xenograft mouse model. (A) Representative photographs of mice at the end of the treatment period. (B) Excised tumors from mice belonging to each treatment group. (C) Tumor growth curves. (D) Body weight changes in tumor-bearing mice during the course of treatment. (E) Histopathological evaluation of tumor tissues *via* hematoxylin and eosin (H&E) staining. (F) TUNEL staining of tumor tissues (green: TUNEL-positive apoptotic cells; blue: DAPI-stained nuclei). (a) Saline, (b) free GEM, (c) GEM@HA-(HAP/PSI)$_{10}$. Data are presented as the mean ± standard deviation ($n \geq 3$). ***$p < 0.001$, ****$p < 0.0001$.

GEM@HA-(HAP/PSI)$_{10}$ demonstrated the most potent antitumor effect. Quantitative analysis (Fig. 7C) confirmed that the HA-modified nano-formulation inhibited tumor growth more effectively than free GEM. Notably, the body weights of mice were comparable between all drug-treated groups and the normal group (Fig. 7D), demonstrating the good biocompatibility and minimal acute systemic toxicity of the prepared nano-formulation at the administered dose.

H&E staining (Fig. 7E) revealed the presence of distinct histopathological alterations in tumor tissues following treatment with both free GEM and the GEM-loaded nano-formulation (GEM@HA-(HAP/PSI)$_{10}$) when compared to the control. In the saline group (Fig. 7E(a)), tumor cells exhibited a highly dense, monomorphic proliferation pattern characterized by a high nuclear-to-cytoplasmic ratio and hyperchromatic nuclei. With their minimal stromal components, the cells grew in the form of solid, back-to-back sheets. This morphology was typical of an untreated, highly proliferative tumor, where uniform cellularity reflects vigorous clonal expansion, and there was no evidence of therapy-induced differentiation or necrosis. In the free GEM group (Fig. 7E(b)), a moderate reduction in overall cellular density was observed. Scattered, small, and structureless eosinophilic areas, indicative of early or focal tumor cell necrosis, were present within the tissue. While the remaining viable cells retained some degree of atypia, signs of active proliferation were reduced. These findings suggested that free GEM exerts a limited and heterogeneous cytotoxic effect, resulting in partial tumor cell death. Notably, no widespread and significant vacuolization was detected in the free GEM group. In contrast, the GEM@HA-(HAP/PSI)$_{10}$ group (Fig. 7E(c)) presented a markedly different histopathological landscape dominated by numerous clear vacuoles, with an overall sparse cellular distribution. These "ghost" outlines were characteristic of coagulative necrosis, signifying extensive cellular disintegration.[52] The residual tumor cell nests appeared fragmented and sparse, indicating widespread, coordinated tumor cell death (including both necrosis and apoptosis) and severe architectural disruption. Notably, the presence of large, confluent necrotic areas is a gold-standard pathological indicator of potent chemotherapeutic efficacy.[53] The extensive vacuolization and necrosis detected in the nano-formulation group suggested that GEM@HA-(HAP/PSI)$_{10}$ facilitates the deeper and more effective accumulation of GEM within tumor tissues, likely through the EPR effect and/or active targeting. The profound reduction in cellularity reflected a substantial decrease in overall tumor burden and suppression of proliferative activity.

To further evaluate the *in vivo* antitumor mechanism, TUNEL/DAPI staining of tumor tissues was performed to detect apoptosis (Fig. 7F and G). In the saline group (Fig. 7F(a)), the TUNEL (red) channel showed intense, dense red fluorescent signals, indicating widespread DNA fragmentation and, consequently, active apoptosis. Meanwhile, the DAPI (blue) channel revealed a high density of nuclei. The extensive co-localization of red signals with blue nuclei (appearing pink/purple) in the merged image confirmed that these apoptotic events occurred within tumor cells. According to the literature, in rapidly growing, highly crowded, untreated tumors, severe nutrient competition and a hypoxic microenvironment can trigger "spontaneous apoptosis" in a subset of cells.[54] However, since the proliferation rate far exceeds the apoptosis rate, the overall tumor mass continues to expand. Therefore, the strong TUNEL signal in this group reflected a "high turnover rate" and internal turmoil (*i.e.*, "background apoptosis" due to internal stress in unperturbed tumors), rather than an effective therapeutic response. In the free GEM group (Fig. 7F(b)), the intensity and density of the TUNEL red signals were reduced when compared to the saline group but were still clearly discernible. The merged image also showed decreased co-localization signals. This indicated that free GEM effectively disrupted DNA synthesis, inducing apoptosis in a portion of tumor cells and potentially clearing some cells, producing a definite pharmacologic effect. However, likely due to factors such as suboptimal drug delivery efficiency and tumor heterogeneity, apoptosis induction was focal and incomplete, failing to destroy most of the tumor tissue.[55] This was consistent with the absence of large necrotic areas in H&E-stained sections. However, the GEM@HA-(HAP/PSI)$_{10}$ group (Fig. 7F(c)) presented the most distinct phenotype. The TUNEL red signal became extremely faint and sparse in this group and was nearly at background levels. This suggested that cells may be undergoing other forms of death on a large scale, such as necrosis or pyroptosis, or that apoptotic cells may be rapidly cleared after the death program was completed, preventing the accumulation of TUNEL-detectable signals. This observation was entirely in line with the extensive necrotic areas observed in H&E staining (Fig. 7E(c)), collectively proving that the nano-formulation triggers a more thorough and widespread disintegration of tumor tissues.

In summary, the antitumor efficacy of the GEM@HA-(HAP/PSI)$_{10}$ nano-formulation was significantly superior to that of the commercially available GEM formulation (free GEM) tested in this study. The superior outcomes likely stemmed from the combined advantages of the nano-formulation: HA-mediated active targeting towards CD44-expressing tumor cells, the passive accumulation facilitated by the EPR effect due to an appropriate nanoscale size (~185 nm), and pH-responsive drug release within the tumor microenvironment or cellular compartments. The commercially available GEM formulation, as a free drug, was distributed non-specifically in the body, was rapidly cleared, and achieved limited accumulation within the tumor tissue. Consequently, it could only induce focal and incomplete tumoricidal effects. In contrast, the GEM@HA-(HAP/PSI)$_{10}$ nano-carrier, owing to the CD44 targeting capacity of HA and its optimal size, achieved highly efficient accumulation at the tumor site *via* the EPR effect and active targeting. This accumulation potentially arose from a combination of: (i) HA–CD44 binding, aiding the anchoring of nanoparticles on CD44-expressing tumor cells during systemic circulation, and (ii) the synergy between the EPR effect and receptor-mediated endocytosis, enabling a higher degree of dual targeting at both the tissue and cellular levels. This resulted in significantly higher local drug concentrations within the tumor, leading to more potent and extensive tumoricidal action. Furthermore, the nanocarrier likely provided protection to GEM, reducing its

rapid metabolic deamination and inactivation in the bloodstream, and could also bypass some membrane transporter-mediated resistance mechanisms *via* endocytic uptake routes. This prolonged drug action likely contributed to more profound and continuous tumor cell death, pathologically manifesting as large areas of tissue disintegration rather than sporadic focal necrosis.

Although a vast array of nanocarriers has been developed, their clinical translation has remained limited. Following the approval of the first PEGylated doxorubicin liposome, Doxil®, in 1995, only approximately 90 nanomedicines had reached the market by the end of 2023,[56] with some even being withdrawn subsequently. At present, the nanocarriers used in clinical settings and those under clinical investigation are still predominantly passively targeted, lipid-based systems. While these nanomedicines have improved patient compliance when compared to conventional formulations, most have not yielded substantial enhancements in clinical efficacy.[57] Meanwhile, more precisely targeted delivery systems, such as those employing active targeting strategies, often encounter significant bottlenecks during clinical development and face translational challenges.[58] In this context, major hurdles include the inherent limitations of nanoparticles with respect to long-term stability, efficacy, and safety; the restricted repertoire of pharmaceutically acceptable carrier materials; and the challenges associated with industrial-scale manufacturing, packaging, and cost-effectiveness. The design, synthesis, and preparation of advanced delivery systems (*e.g.*, active, physical, or chemical targeting) are often complex, leading to difficulties in reproducible scale-up production, stringent impurity/quality control, and adequate sterilization and physicochemical stability. These issues collectively represent a key hurdle in the journey from the development of functional nanocarriers to their successful industrial and clinical translation.

In this context, the GEM@HA-(HAP/PSI) nano-targeted delivery system developed in this study presents several potential advantages for clinical translation when compared to conventional liposomal formulations. These include its relatively lower production costs (owing to the use of inexpensive raw materials), a simple and feasible preparation process that does not require stringent conditions or specialized equipment, minimal impurity generation, the feasibility of integrating sterilization during excipient production, ease of terminal sterilization, and considerable process robustness (such that variations in feed quantities within a certain range do not compromise product quality). Furthermore, the system currently has a DLC of at least 300 mg g^{-1}. The platform developed in this study is thus highly promising from a clinical perspective. By modulating the shell materials, core composition, and particle size, this system may be adapted for different targeting modalities (passive, active, physical, or chemical) and could be suitable for various administration routes, including oral administration, inhalation, implantation, and injection. Overall, this delivery system appears to be particularly well-suited for the *in vivo* delivery of antitumor agents and nucleic acid-based gene therapeutics.

4. Conclusion

In this study, based on a CD44 receptor-mediated active targeting strategy, we successfully developed a HA-modified nanocarrier co-delivery system, termed GEM@HA-(HAP/PSI), for the encapsulation of GEM. The resulting nanoparticles showed spherical morphology, uniform distribution, and a moderately negative surface charge. *In vitro* cellular uptake studies demonstrated that the system could effectively enhance intracellular accumulation in CD44-overexpressing lung cancer cells *via* HA–CD44 receptor interaction, which confirmed its active targeting capability. More importantly, *in vivo* antitumor efficacy assessments indicated that GEM@HA-(HAP/PSI) provides significantly stronger tumor growth inhibition than free GEM or a commercial GEM formulation. Collectively, this study offers a promising targeted delivery strategy for GEM in cancer therapy.

Author contributions

Fengbo Yu: investigation, funding acquisition, writing – review & editing, conceptualization. Jingdan Cao: investigation, methodology, data curation. Xingjun Fan: methodology, data curation. Junxia Gao: methodology, data curation. Guifang Liu: investigation, methodology, formal analysis. Chonghuan Lin: investigation, methodology, data curation. Ying Zhu: investigation, methodology. Qiang Wang: funding acquisition, writing – original draft, data curation.

Conflicts of interest

The authors declare that they have no known competing financial interests or personal relationships that could have appeared to influence the work reported in this paper.

Data availability

Data will be made available on request.

Supplementary information (SI): (1) UV-vis scanning spectra and standard curve of gemcitabine (GEM). (2) HPLC chromatograms of HA-PSI at different reaction time points. (3) FT-IR and SEM characterization of HAP. (4) SEM analysis of HA-PSI/HAP ratios in self-assembled nanoparticles. (5) results of single-factor optimization experiments. (6) concentration optimization of GEM@(HAP/PSI) and GEM@HA-(HAP/PSI) formulations. See DOI: https://doi.org/10.1039/d6ra02076c.

Acknowledgements

This work was supported by Heilongjiang Provincial Natural Science Foundation of China [grant number SS2024H002].

References

1 Y. Teng, X. Zhang, C. Xia and W. Chen, *China J. Cancer Prev. Treat.*, 2024, **31**, 1413–1420, DOI: 10.16073/j.cnki.cjcpt.2024.23.01.

2 B. Han, R. Zheng, H. Zeng, S. Wang, K. Sun, R. Chen, L. Li, W. Wei and J. He, *J. Natl. Cancer Cent.*, 2024, **4**, 47–53, DOI: 10.1016/j.jncc.2024.01.006.
3 A. Płużański and A. Piórek, *Oncol. Clin. Pract.*, 2025, **21**, 370–376, DOI: 10.5603/ocp.100477.
4 L. B. Pang, J. Li, Z. W. Zhang and C. Q. Zhang, *Eur. Cells Mater.*, 2025, **50**, 87–108, DOI: 10.22203/eCM.v050a06.
5 C. Jiang, S. Xie, K. Jia, G. Feng, X. Ren and Y. Wang, *J. Pharm. Anal.*, 2025, **15**, 101179, DOI: 10.1016/j.jpha.2024.101179.
6 P. Jain, H. Kathuria and M. Momin, *Pharmacol. Ther.*, 2021, **226**, 107871, DOI: 10.1016/j.pharmthera.2021.107871.
7 M. J. Mitchell, M. M. Billingsley, R. M. Haley, M. E. Wechsler, N. A. Peppas and R. Langer, *Nat. Rev. Drug Discovery*, 2021, **20**, 101–124, DOI: 10.1038/s41573-020-0090-8.
8 C. Salvador-Morales and P. Grodzinski, *ACS Nano*, 2022, **16**, 5062–5084, DOI: 10.1021/acsnano.1c10635.
9 N. Zheng, Q. Wang, S. Zhang, C. Mao, L. He and S. Liu, *J. Mater. Chem. B*, 2022, **10**, 7450–7459, DOI: 10.1039/d2tb00935h.
10 A. Paris, N. Tardif, M. D. Galibert and S. Corre, *Int. J. Mol. Sci.*, 2021, **22**, 752, DOI: 10.3390/ijms22020752.
11 A. J. Rozo, M. H. Cox, A. Devitt, A. J. Rothnie and A. D. Goddard, *Methods*, 2020, **180**, 45–55, DOI: 10.1016/j.ymeth.2020.05.001.
12 S. Shen, H. Lu, L. Liu, Y. Wang, C. Zhang, W. Yang and W. Xu, *Oral Dis.*, 2020, **26**, 47–557, DOI: 10.1111/odi.13279.
13 R. Lee, Y. J. Choi, M. S. Jeong, Y. Park, K. Motoyama, M. W. Kim, S. Kwon and J. H. Choi, *Bioconjugate Chem.*, 2020, **31**, 923–932, DOI: 10.1021/acs.bioconjchem.0c00048.
14 S. Ghosh, S. Dutta, A. Sarkar, M. Kundu and P. Sil, *Colloids Surf., B*, 2021, **197**, 111404, DOI: 10.1016/j.colsurfb.2020.111404.
15 S. Köse, B. Kankilic, M. Gizer, E. C. Dede, E. Bayramli, P. Korkusuz and F. Korkusuz, *Adv. Exp. Med. Biol.*, 2018, **1077**, 317–342, DOI: 10.1007/978-981-13-0947-2_17.
16 K. Balagangadharan, S. V. Chandran, B. Arumugam, S. Saravanan, G. Devanand Venkatasubbu and N. Selvamurugan, *Int. J. Biol. Macromol.*, 2018, **111**, 953–958, DOI: 10.1016/j.ijbiomac.2018.01.122.
17 J. Velazco-de-la-Garza, L. Averous, G. de Jesus Sosa-Santillan, E. Pollet, A. Zugasti-Cruz, C. A. Sierra-Rivera, N. V. Pérez-Aguilar and E. Oyervides-Muñoz, *Eur. Polym. J.*, 2020, **131**, 109705, DOI: 10.1016/j.eurpolymj.2020.109705.
18 E. Jalalvandi and A. Shavandi, *Eur. Polym. J.*, 2018, **109**, 43–54, DOI: 10.1016/j.eurpolymj.2018.08.056.
19 J. Vega-Chacón, R. D. Piazza, R. F. C. Marques, A. Elaissari and M. Jafelicci, *Polym. Int.*, 2019, **68**, 88–93, DOI: 10.1002/pi.5699.
20 S. S. Agrawal, V. Baliga and V. Y. Londhe, *Pharmaceutics*, 2025, **17**, 36, DOI: 10.3390/pharmaceutics17010036.
21 M. Sameer Khan, G. Gupta, A. Alsayari, S. Wahab, A. Sahebkar and P. Kesharwani, *Int. J. Pharm.*, 2024, **658**, 124212, DOI: 10.1016/j.ijpharm.2024.124212.
22 J. Gao, W. Zhang, Q. Wang, J. Cao, Y. Zhu, G. Liu, Y. Jia and F. Yu, *Int. J. Pharm.:X*, 2025, **10**, 100431, DOI: 10.1016/j.ijpx.2025.100431.
23 K. Qu, *Design, Synthesis and Activity Study of Tumor-Targeted Gemcitabine Prodrug*, Qilu University of Technology, 2024.
24 A. Gilarska, J. Lewandowska-Łańcucka, K. Guzdek-Zając, A. Karewicz, W. Horak, R. Lach, K. Wójcik, R. Lach, K. Wójcik and M. Nowakowska, *Int. J. Biol. Macromol.*, 2020, **155**, 938–950, DOI: 10.1016/j.ijbiomac.2019.11.052.
25 C. D. Blundell and M. A. C. Reed, Andrew Almond, *Carbohydr. Res.*, 2006, **341**, 2803–2815, DOI: 10.1016/j.carres.2006.09.023.
26 V. Torma, T. Gyenes, Z. Szakács, B. Noszál, Á. Némethy and M. Zrínyi, *Polym. Bull.*, 2007, **59**, 311–318, DOI: 10.1007/s00289-007-0774-9.
27 F. Gürer, T. Mohan, M. Bračič, A. Barlič, D. Makuc, J. Plavec, K. S. Kleinschek and R. Kargl, *Int. J. Biol. Macromol.*, 2024, **274**, 133301, DOI: 10.1016/j.ijbiomac.2024.133301.
28 Y. S. Yang, Y. Zhao, J. S. Lan, Y. N. Kang, T. Zhang, Y. Ding, X. Y. Zhang and L. Lu, *Int. J. Nanomed.*, 2018, **13**, 4361–4378, DOI: 10.2147/IJN.S165359.
29 A. M. A. Pistorius, P. J. T. A. Groenen and W. J. D. Grip, *Int. J. Pept. Protein Res.*, 1993, **42**, 570–577, DOI: 10.1111/j.1399-3011.1993.tb00366.x.
30 M. Zhang, J. Yang, F. Deng, C. Guo, Q. Yang, H. Wu, Y. Ni, L. Huang, L. Chen and C. Ding, *Carbohydr. Polym.*, 2019, **215**, 358–365, DOI: 10.1016/j.carbpol.2019.03.086.
31 A. Fallacara, F. Marchetti, M. Pozzoli, U. R. Citernesi, S. Manfredini and S. Vertuani, *Pharmaceutics*, 2018, **10**, 254, DOI: 10.3390/pharmaceutics10040254.
32 S. S. Kozlov, V. Alexeeva Olga, B. Nikolskaia Anna, I. Petrova Vasilisa, O. K. Karyagina, L. Iordanskii Alexey, L. Larina Liudmila and I. Shevaleevskiy Oleg, *Polymers*, 2025, **17**, 653, DOI: 10.3390/polym17050653.
33 G. Mohamed, H. A. Hayfa and H. M. Abd El-Lateef, *J. Mater. Res. Technol.*, 2023, **26**, 7925–7935, DOI: 10.1016/j.jmrt.2023.09.086.
34 A. F. Halasa, G. D. Wathen, W. L. Hsu, B. A. Matrana and J. M. Massie, *J. Appl. Polym. Sci.*, 1991, **43**, 183–190, DOI: 10.1002/app.1991.070430115.
35 P. Gawali, A. Saraswat, S. Bhide, S. Gupta and K. Patel, *Nanomedicine*, 2023, **18**, 169–190, DOI: 10.2217/nnm-2022-0257.
36 B. Du, M. Yu and J. Zheng, *Nat. Rev. Mater.*, 2018, **3**, 358–374, DOI: 10.1038/s41578-018-0038-3.
37 E. Blanco, H. Shen and M. Ferrari, *Nat. Biotechnol.*, 2015, **33**, 941–951, DOI: 10.1038/nbt.3330.
38 C. van Ballegooie, A. Man, I. Andreu, B. D. Gates and D. Yapp, *Processes*, 2019, **7**, 290, DOI: 10.3390/pr7050290.
39 D. L. Lam, Y. T. Cheng and C. J. Huang, *ACS Appl. Mater. Interfaces*, 2023, **15**, 53297–53309, DOI: 10.1021/acsami.3c12939.
40 K. A. White, B. K. Grillo-Hill and D. L. Barber, *J. Cell Sci.*, 2017, **130**, 663–669, DOI: 10.1242/jcs.195297.
41 N. N. N. Maarof, E. Abdulmalek, S. Fakurazi and M. B. A. Rahman, *Pharmaceutics*, 2022, **14**, 1230, DOI: 10.3390/pharmaceutics14061230.
42 A. D'Ambrosio, S. Scialla, V. Piemonte, D. Moscatelli and E. Mauri, *Mol. Pharm.*, 2025, **22**, 6611–6622, DOI: 10.1021/acs.molpharmaceut.5c00494.

43 ASTM International, *Standard Practice for Assessment of Hemolytic Properties of Materials*, ASTM F756-17, West Conshohocken, PA, 2017.
44 S. Malehmir, M. A. Esmaili, M. Khaksary Mahabady, A. Sobhani-Nasab, A. Atapour, M. R. Ganjali and A. Ghasemi, Moradi Hasan-Abad A, *Front. Chem.*, 2023, **11**, 1249134, DOI: 10.3389/fchem.2023.1249134.
45 Y. Li, M. Zhang, Y. Zhang, X. Niu, Z. Liu, T. Yue and W. Zhang, *J. Mater. Chem. B*, 2023, **11**, 6319–6334, DOI: 10.1039/D3TB00322A.
46 G. J. Doherty and H. T. McMahon, *Annu. Rev. Biochem.*, 2009, **78**, 857–902, DOI: 10.1146/annurev.biochem.78.081307.110540.
47 A. L. Kiss, Erzsébet Botos, *J. Cell. Mol. Med.*, 2009, **13**, 1228–1237, DOI: 10.1111/j.1582-4934.2009.00754.x.
48 A. Dagmar, D. V. Kuhn, M. Benjamin, F. Blank, P. Gehr, A. Petri-Fink and B. Rothen-Rutishauser, *Beilstein J. Nanotechnol.*, 2014, **5**, 1625–1636, DOI: 10.3762/bjnano.5.174.
49 A. Almalik, S. Karimi, S. Ouasti, R. Donno, C. Wandrey, P. J. Day and N. Tirelli, *Biomaterials*, 2013, **34**, 5369–5380, DOI: 10.1016/j.biomaterials.2013.03.065.
50 J. Wang, N. Muhammad, T. Li, H. Wang, Y. Liu, B. Liu and H. Zhan, *Mol. Pharm.*, 2020, **17**, 2411–2425, DOI: 10.1021/acs.molpharmaceut.0c00161.
51 S. Paroha, R. D. Dubey, J. Verma, V. Jain, S. Akbar, A. K. Mishra, S. L. Neha, L. Rani, A. Kumar Mahto, P. Kumar Sahoo and R. Prasad Dewangan, *Curr. Drug Delivery*, 2025, **22**, 1430–1440, DOI: 10.2174/0115672018317615240926163652.
52 S. A. Elmore, D. Dixon, J. R. Hailey, T. Harada, R. A. Herbert, R. R. Maronpot, T. Nolte, J. E. Rehg, S. Rittinghausen, T. J. Rosol, H. Satoh, J. D. Vidal, C. L. Willard-Mack and D. M. Creasy, *Toxicol. Pathol.*, 2016, **44**, 173–188, DOI: 10.1177/0192623315625859.
53 R. Salgado, C. Denkert, S. Demaria, N. Sirtaine, F. Klauschen, G. Pruneri, S. Wienert, E. G. Van den, F. L. Baehner, F. Penault-Llorca, E. A. Perez, E. A. Thompson, W. F. Symmans, A. L. Richardson, J. Brock, C. Criscitiello, H. Bailey, M. Ignatiadis, G. Floris, J. Sparano, Z. Kos, T. Nielsen, D. L. Rimm, K. H. Allison, J. S. Reis-Filho, S. Loibl, C. Sotiriou, G. Viale, S. Badve, S. Adams, K. Willard-Gallo and S. Loi, *Ann. Oncol.*, 2014, **26**, 259–271, DOI: 10.1093/annonc/mdu450.
54 P. Vaupel and A. Mayer, *Cancer Metastasis Rev.*, 2007, **26**, 225–239, DOI: 10.1007/s10555-007-9055-1.
55 M. Ye, J. Hu, L. Han, H. Zhang, X. Peng, Y. Kang, S. Bai and Z. Xu, *Advanced Science*, 2024, **11**, 2402809, DOI: 10.1002/advs.202402809.
56 Y. Jiang, Y. He, W. Zhang, J. Zou, K. Magar, H. Boucetta, C. Teng and W. He, *Pharmaceutics*, 2023, **15**, 774, DOI: 10.3390/pharmaceutics15030774.
57 R. Zingg and M. Fischer, *Wiley Interdiscip. Rev.:Nanomed. Nanobiotechnol.*, 2019, **11**, e1569, DOI: 10.1002/wnan.1569.
58 D. Rosenblum, N. Joshi, W. Tao, J. M. Karp and D. Peer, *Nat. Commun.*, 2018, **9**, 1410, DOI: 10.1038/s41467-018-03705-y.